Draft Manuscript for Review

POD-based reduced order model for the prediction of global and local elastic responses of fibre-reinforced polymer considering varying fibre distribution

Journal:	*Computational Mechanics*
Manuscript ID	CM-22-0390.R1
Manuscript Type:	Original Paper
Date Submitted by the Author:	26-Jan-2023
Complete List of Authors:	Jamnongpipatkul, Arada; KU Leuven, Department of Mechanical Engineering; Ghent University, Department of Materials, Textiles and Chemical Engineering Sevenois, Ruben; Ghent University, Department of Materials, Textiles and Chemical Engineering Desmet, Wim; KU Leuven, Department of Mechanical Engineering Naets, Frank; KU Leuven, Department of Mechanical Engineering Gilabert, Francisco; Ghent University, Department of Materials, Textiles and Chemical Engineering
Keywords:	micro-mechanics, finite element, composite materials, numerical methods
Note: The following files were submitted by the author for peer review, but cannot be converted to PDF. You must view these files (e.g. movies) online.	
rev2_manuscript_CM_2cols.tex rev2_refs.bib sn-jnl.cls sn-mathphys.bst	

POD-based reduced order model for the prediction of global and local elastic responses of fibre-reinforced polymer considering varying fibre distribution

A.Jamnongpipatkul[1,2,3,4*], R.D.B. Sevenois[3], W. Desmet[1,4], F. Naets[1,4] and F.A. Gilabert[3]

[1]Division LMSD, Department of Mechanical Engineering, KU Leuven, Celestijnenlaan 300, Heverlee, 3001, Belgium.
[2]SIM M3 program, Technologiepark 48, Zwijnaarde, B-9052, Belgium.
[3]Mechanics of Materials and structures, Department of Materials, Textiles and Chemical Engineering, Ghent University, Technologiepark 46, Zwijnaarde, B-9052, Belgium.
[4]DMMS Lab, Flanders Make at KU Leuven, Belgium.

*Corresponding author(s). E-mail(s): arada.jamnongpipatkul@kuleuven.be;

Abstract

Computational homogenization is commonly used to predict the responses of composite materials. However, it poses practical issues due to large computational cost especially in the material-by-design setting when various design parameters are to be examined. This paper presents the development of a parametric model order reduction strategy for the micromechanical analysis of composites when fibre distribution is the parameter of interest. The reduced order model is obtained by applying Galerkin projection in combination with proper orthogonal decomposition. The presented framework enables a significantly reduced computational load during parametric studies as the model dimension of the microscale analyses is significantly smaller. The results show that the proposed approach can reproduce the homogenized properties of material and local stress distributions in the microstructures very well.

Keywords: Fibre reinforced polymer (FRP), Micromechanics, Parametric model order reduction, Proper Orthogonal Decomposition, Finite element method

1 Introduction

Fibre reinforced polymer composites (FRP) have gained popularity in many engineering sectors because of their ability to be tailored to desirable mechanical properties suitable in a wide variety of applications like in aerospace, automobile, medicine, energy, etc. However, designing such composite materials is a repetitive process. Designers need to investigate numerous combinations of various design parameters until the desirable mechanical properties at the structural level are obtained. For heterogeneous materials such as FRP, predicting these properties is accomplished through multiscale analysis. In multiscale analysis, material behaviour of each constituent is modelled at the microscale, after which the homogenized macromechanical behaviour is obtained through volume averaging.

FRP exhibits a heterogeneous composition at micro- and mesoscale but can be regarded as homogeneous at the macroscale as shown in Figure 1. At the microscale, for example, unidirectional (UD) FRP is modelled as an isotropic matrix reinforced with cylindrical fibres aligned in their longitudinal direction with the diameter of each fibre in the range of micrometers. The mesoscale with the dimension in the range of millimeters is an intermediate scale for modelling more complicated architectures like woven [1] or braided [2] composites, where the yarns are modelled as homogenized fibre bundles similar to UD plies. Finally, at the macroscale or the structural level, FRP consists in a laminated structure with the dimension in the range of centimeters and above.

When there is a clear separation of length scales, the composite behaviour is studied through the simulation at each scale that can be carried out separately starting from the microscale. To represent the composite microstructure at the microscale, a representative volume element (RVE) is generated. The fibres and matrix are distinguished and modelled in detail in the RVE. The result from the RVE simulation is homogenized and passed to the simulation of the next length scale. Consequently, the overall response at the macroscale is driven by what happens at the microscale.

Analyzing the microscopic problem associated to the RVE can be done by computational tools such as the finite element method (FEM). Generally, a fine mesh leading to large number of degrees of freedom and large system of equations is required to get accurate solutions. As a result, the simulation of a microstructure is computationally demanding. When numerous simulations with fine discretization are to be performed over different design parameter values, the task becomes computationally infeasible.

Model order reduction (MOR) is an efficient numerical approach that can be used to reduce the dimension of the problem. As a result, the computational cost is reduced significantly without compromising the solution accuracy. MOR has been applied successfully in many engineering applications such as fluid dynamics [3], structural dynamics [4], optimization [5], uncertainty quantification [6], among others. Depending on the problem nature, many approaches and methodologies are proposed. Soldner et al. [7] compared multiple MOR techniques applied to the microscopic boundary value problem of a RVE with a single inclusion. The general idea of MOR concerns the construction of a reduced order model (ROM) using information obtained from one or more simulations of a full order model (FOM) at one or more design parameter values. The resulting ROM can then replace the FOM to assess other design parameters. The FOM may refer to a finite element model as is the case in this paper.

For composites, design parameters can be generally categorized into three groups: material parameters, loading parameters and microstructural geometrical parameters. Goury et al.[8] developed a sampling strategy for the parameter space represented by any load path applied onto the RVE. A reliable ROM was built and illustrated in the context of elastic-damageable particular composites. Tuijl et al. [9] also focused on the loading parameters while keeping the material parameter and microstructural geometrical parameter unchanged. They compared two MOR techniques on approximating the micro- and macroscopic quantities of interest when the RVE was subjected to the load case that includes unsampled states of the history parameters. Raschi et al.[10] applied reduced order modelling with optimal cubature to finite element square (FE^2) technique. They compared the homogenized stresses obtained from the FOM and the ROM for a particular loading trajectory that was not considered during the sampling stage. They also showed the capability of the ROM to accommodate changes in the material parameters characterizing the composite phases. The ROM was developed using a given composite morphology and a given set of material parameters. It was then used to predict the responses of the composites having the same morphology and governed by the same material constitutive model but with remarkably different values of material properties with respect to those adopted during the sampling stage. However, to the authors' knowledge, application of MOR with microstructural morphology as design parameter is still missing in the field of composite analysis.

Varying morphology of fibre reinforced composites at microscale such as fibre clustering or

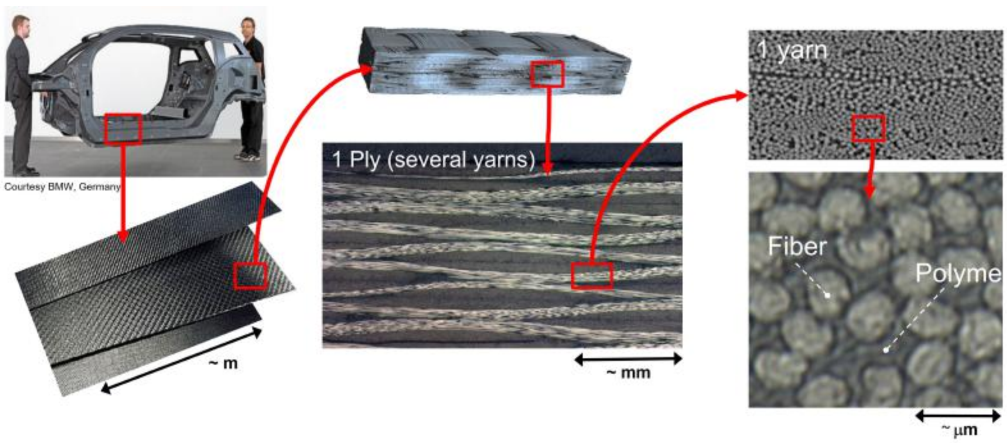

Fig. 1: Length scales involved in multiscale modelling of the FRPs

matrix-rich regions may occur during the manufacturing process [11]. Studies show that the heterogeneity of the reinforcement at microscale affects stress distributions at the microstructural level [12], interface stress distribution [13], transverse crack formation [14], transverse creep behaviour [15] and effective elastic properties [16]. It is therefore essential to have a thorough understanding of the effect of the spatial distribution of fibres on the response of composite material in both linear and nonlinear regime. In the linear regime, the analytical methods such as the Halpin-Tsai model [17] or Chamis' formulae [18], among others, are efficient to predict the effective elastic properties of the material. However, these methods do not provide local responses in the microstructure. As a result, the effect of the spatial distributions of fibres on the local responses such as stress distributions cannot be captured by these methods. The direct numerical simulation via finite element analysis is needed. Generally, one would perform numerical simulation on one large RVE [19, 20] that demonstrates the convergence in the macroscopic response. It is considered to sufficiently represent randomness in the microstructure. This practice is reasonable when the aim is to study the global behavior of the composites.

However, the study from Jiménez [21] shows that there are significant variations in microscopic fields among 200 different random realizations of the RVE with the same macroscopic properties, particularly in the regions of high strain and stress concentrations. These variations can lead to different damage and failure behavior of the composites. Including processes such as plasticity and fracture in the analysis increases significantly the computational cost which prevents the comprehensive investigation. Yin and Pindera [22] tried to address this issue by proposing a hybrid homogenization theory that combines elements of finite volume and locally-exact elasticity approaches. Their proposed methodology achieves greater reductions in execution times relative to the finite volume micromechanics. The development of MOR framework proposed in this work is the alternative to help reducing the computational cost and broaden the investigations on the effect of varying fibre distributions on local behavior of the composites. Though the proposed strategy is applied to linear regime in this paper, it paves the way for the application in nonlinear regime in the future.

This work addresses some fundamental issues in MOR, namely sampling of the parametric space, intrusiveness, error estimation and handling geometrical parameter. The proposed solutions are tailored for the MOR application on the analysis of composite material with fibre distribution as the design parameter. The proposed MOR framework uses the proper orthogonal decomposition (POD) to construct a reduced order basis (ROB) and the Galerkin projection to formulate a ROM. This MOR approach has proved to be very successful to study different aspects of material modeling, such as the heat conduction in composites [23] or the hyperelastic response in porous elastomers [24].

However, when the design parameter involves geometric features like the fibre distribution, usual POD-based procedures cannot be carried out due to the different spatial discretizations. To overcome this issue, a premeshed RVE strategy is proposed. This strategy makes it possible to generate different fibre distributions without altering the mesh topology. Once the process to construct a ROB can be carried out, the next step is to construct a ROB that represents the physical characteristics of the problem. For this, the microstructural ranking indicator is established to ensure that those microstructures with different geometrical characteristics are taken into account in the construction of the ROB. Lastly, POD-based approach does not provide any information on the accuracy of the solution obtained from the ROM. In this work, the internal forces in the FEM domain of the RVE is monitored and used to determine the state of the ROM solution. To assess the capability of the proposed methodology, the comparison of the homogenized elastic properties and stress distributions obtained from the FOM and the ROM are presented.

This paper is organized as follows. Section 2 presents an overview of the multiscale problem, its discretization by the FEM and the Galerkin-POD based MOR approach applied to the problem at microscale. The resolutions to the issues arisen from applying Galerkin-POD based MOR approach to the analysis of UD composites at microscale are detailed in Section 3. Section 4 presents the assessment of the accuracy and efficiency of the developed ROM by comparing the global and local responses of microstructures with the FE simulations. Concluding remarks are provided in Section 5.

2 Model order reduction for multiscale computational homogenization

This section gives a brief introduction to the multiscale computational homogenization and the implementation of the projection-based MOR.

2.1 Multiscale computational homogenization

Computational homogenization procedure will be outlined for the UD-based laminates in this work. As a result, modelling of such composite structure becomes a two-scale problem where the characteristic length at microscale l^μ is very small compared to the macroscopic length scale l. This separation of length scales is the underlying assumption of the first-order computational homogenization [25]. Under this framework, the problem describing the response of a structure driven by the heterogeneous microstructure can be decomposed into two boundary value problems at microscale and macroscale.

At the microscale, the displacement at point $\mathbf{x}$ can be split as:

$$\mathbf{u}^\mu(\mathbf{x}) = \bar{\mathbf{u}}(\mathbf{x}) + \tilde{\mathbf{u}}^\mu(\mathbf{x}). \tag{1}$$

where $\bar{\mathbf{u}}$ is the displacement induced by the macroscopic strain $\bar{\boldsymbol{\varepsilon}}$ defined as $\bar{\boldsymbol{\varepsilon}} \cdot \mathbf{x}$ and $\tilde{\mathbf{u}}^\mu$ is the displacement fluctuation. Assuming small-strain kinematics, the microscopic strain $\boldsymbol{\varepsilon}^\mu$ is then given by the symmetric gradient of the displacement at the microscale:

$$\boldsymbol{\varepsilon}^\mu(\mathbf{x}) = \nabla^s \mathbf{u}(\mathbf{x})^\mu = \bar{\boldsymbol{\varepsilon}} + \tilde{\boldsymbol{\varepsilon}}(\mathbf{x}), \tag{2}$$

where $\tilde{\boldsymbol{\varepsilon}}(\mathbf{x}) = \nabla^s \tilde{\mathbf{u}}^\mu(\mathbf{x})$ is the strain fluctuation. Note that the superscript μ indicate the variables at the microscale.

The displacement vector field at the microscale $\mathbf{u}^\mu$ is governed by the equilibrium condition along with the well-posed boundary condition. In the absence of a body force, the equilibrium condition at the microscale is described as:

$$\operatorname{div} \boldsymbol{\sigma}^\mu = \mathbf{0}, \tag{3}$$

where $\boldsymbol{\sigma}^\mu$ is the microscopic stress.

The problem has to be completed by the constitutive relations of the constituents. In this work, the materials are considered linear elastic which can be defined as:

$$\boldsymbol{\sigma}^\mu = \mathbb{C}^{(\mathrm{r})} : \boldsymbol{\varepsilon}^\mu, \tag{4}$$

where $\mathbb{C}^{(\mathrm{r})}$ is the fourth-order elasticity tensor of phase r. The material properties of each phase are known at the microscale.

The relationship between the microscale and the macroscale is established based on two principles. The first principle states that the volume average of the microscopic strain $\boldsymbol{\varepsilon}^\mu$ is equivalent to the macroscopic strain $\bar{\boldsymbol{\varepsilon}}$:

$$\bar{\boldsymbol{\varepsilon}} = \frac{1}{V^\mu}\int_{\Omega^\mu} \boldsymbol{\varepsilon}^\mu \mathrm{d}\Omega^\mu. \tag{5}$$

where Ω^μ is a heterogeneous microstructure with a volume V^μ.

The second principle is through the adoption of the Hill-Mandel condition [26, 27]. It states the equality of the virtual work per unit volume at macroscale and the volume average of the virtual work at microscale:

$$\boldsymbol{\sigma} : \delta\boldsymbol{\varepsilon} = \frac{1}{V^\mu}\int_{\Omega^\mu} \boldsymbol{\sigma}^\mu. : \delta\boldsymbol{\varepsilon}^\mu \mathrm{d}\Omega^\mu. \tag{6}$$

Consequently, the macroscopic stress $\boldsymbol{\sigma}$ can be obtained as the volume average of the microscopic stress:

$$\boldsymbol{\sigma} = \frac{1}{V^\mu}\int_{\Omega^\mu} \boldsymbol{\sigma}^\mu \mathrm{d}\Omega^\mu. \tag{7}$$

The Hill-Mandel condition is ensured by imposing periodic boundary conditions (PBCs) [28].

When a RVE is used to represent the composite microstructure, applying PBCs also prevents border effects and makes it possible to use such a small simulation domain to represent the mechanical state of the linear structure [29]. The following formulation describes the relative displacement between the opposing faces of the RVE due to the imposed PBCs:

$$u_j^{i+} - u_j^{i-} = \varepsilon_{ij} l_i \qquad (i, j = x, y, z), \tag{8}$$

where ε_{ij} is the component of the macroscopic strain, l_i is the length of the RVE between the opposite faces in the i-direction and u_j^* is the displacement in $j-$degree of freedom on the indicated face in the i-direction. Following the notations in Figure 2, the surface BCGF, namely x^+ face, corresponds to the yz-plane at the side of the RVE on the positive x-axis. Its counterpart, x^- face, is at the side of the RVE on the negative x-axis aligned with the surface ADHE. The definition for the other faces follows the same reasoning. When the lengths of the RVE l_i are fixed, the term $\varepsilon_{ij} l_i$ can be regarded as the displacement component j of a reference point. The nodes at the vertices B, D and E (see Figure 2) are used as a reference point for linking nodes in opposite x-, y- and z-faces, respectively. When the macroscopic strain tensor $\boldsymbol{\varepsilon}$ is specified, Equation (8) describes the nodal displacement constraints that replicate a desired load case. Note that the set of equation (8) requires a conformal mesh such that PBCs can be imposed on all nodes on one surface and their counterpart nodes on the opposite face as shown in Figure 2. A detailed implementation of PBCs on the RVE can be found in [30].

Once the domain's boundary conditions are established, the multiscale computational homogenization problem now reduces to the resolution of the displacement in a RVE for a given macroscopic strain $\boldsymbol{\varepsilon}$.

2.2 Enforcement of the periodic boundary conditions in the finite element analysis

Finite element analysis is one of the typical approaches used for the numerical resolution of structural microscale problems. In practice, the boundary conditions can be enforced by one of the following approaches; (i) elimination of dependent degrees of freedom, (ii) the penalty method or (iii) Lagrange multipliers [31]. When looking at the PBC formulation in Equation (8), it is intuitive and straightforward to enforce PBCs by Lagrange multipliers. When imposing the constraints via Lagrange multipliers, the discretization of the weak form of Equation (3) along with the PBCs (8) leads to the following system of equations:

$$\begin{bmatrix} \mathbf{K}(p) & \mathbf{G}^T(p) \\ \mathbf{G}(p) & \mathbf{0} \end{bmatrix} \begin{Bmatrix} \mathbf{u}^\mu(p) \\ \boldsymbol{\lambda}(p) \end{Bmatrix} = \begin{Bmatrix} \mathbf{0} \\ \mathbf{q}(p) \end{Bmatrix}, \tag{9}$$

where $\mathbf{K} \in \mathbb{R}^{N\times N}$ is the unconstrained stiffness matrix, $\mathbf{u}^\mu \in \mathbb{R}^N$ is the nodal displacements at microscale, $\boldsymbol{\lambda} \in \mathbb{R}^{N^c}$ is the vector of Lagrange multipliers which enforce the (periodic boundary) constraints, $\mathbf{G} \in \mathbb{R}^{N^c\times N}$ is the constraint matrix, $\mathbf{q} \in \mathbb{R}^{N^c}$ is the displacement constraint vector due to the macroscopic strain $\boldsymbol{\varepsilon}$, N is the total number of degrees of freedom and N^c is the number of degrees of freedom at which the PBCs are imposed. All these variables depend on the design parameter p, which can be any material parameter, loading parameter and/or microstructural geometrical parameter. For the sake of brevity,

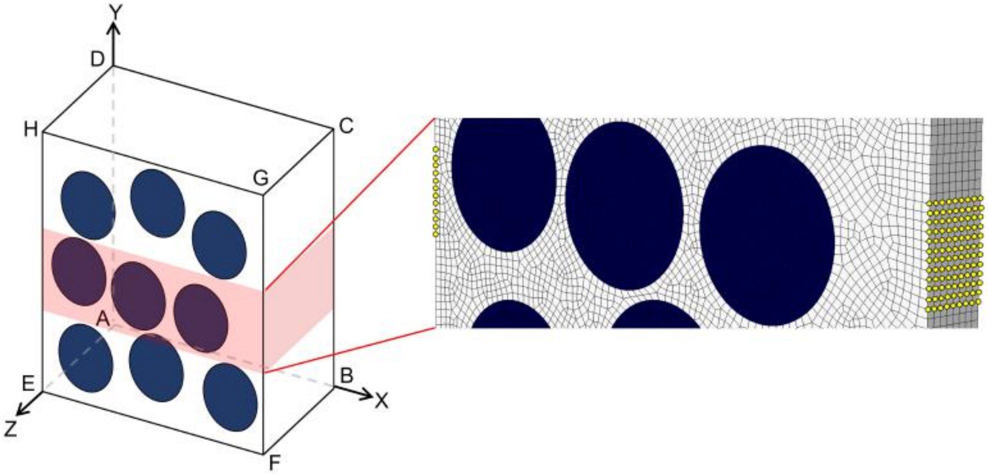

Fig. 2: 3D RVE describing parallel faces and node pairs

The explicit parametric dependence of the variables and the superscript μ indicating the variables at the microscale will be omitted for the remainder of the paper.

The constraint matrix $\mathbf{G}$ consists of N columns equal to the total number of degrees of freedom while the number of rows N^c relates to the number of degrees of freedom at which the PBCs are imposed. One row in the constraint matrix $\mathbf{G}$ stands for one equation in the PBCs from Equation (8). Conforming mesh is used in this work. And under this assumption, the coefficients in each row can be only 1, -1, and 0. The column that corresponds to the degree of freedom on the positive face is equal to 1 while it is -1 for the degree of freedom on the negative face. The coefficient for the remaining degrees of freedom is 0. Equation (10) is an example of the constraint matrix $\mathbf{G}$ like:

$$\mathbf{G} = \begin{bmatrix} & & & & \dots & & & \\ 0 & \dots & -1 & 0 & \dots & 1 & 0 & \dots & 0 \\ 0 & \dots & 0 & 1 & \dots & 0 & -1 & \dots & 0 \\ & & & & \dots & & & \end{bmatrix}. \tag{10}$$

The system of Equation (9) will be referred to as the full order model *FOM*. It has a size of $N + N^c$ which can be very large as a result of the complex geometries and high stress gradients often encountered at the microscale in the composites.

Conventionally, the evaluation of the FOM is carried out for a potentially large set of design parameters of interest. The computed displacement $\mathbf{u}$ corresponding to each design parameter p is referred to as *a snapshot*. The goal of this work is to substitute the FOM with a lower cost ROM by means of projection-based reduced order basis method for several of these parameter samples, as will be outlined in the following sections.

2.3 Model order reduction for a system with periodic boundary conditions

In this work, a projection-based reduced order basis method is applied. The main elements of projection-base reduced order basis methods are the construction of the ROB which is based on the proper orthogonal decomposition (POD) and the projection of the governing equations resulting in a ROM.

Following the displacement decomposition of Equation (1), the need for Lagrange multipliers in the ROM for microscale problems with PBCs can be avoided by assuming that the displacement fluctuation $\tilde{\mathbf{u}}$ equals to:

$$\tilde{\mathbf{u}} = \mathbf{N}\mathbf{u}^{\mathrm{n}}, \tag{11}$$

where $\mathbf{N} \in \mathbb{R}^{N \times (N - N^c)}$ is the null space of the constraint matrix $\mathbf{G}$, such that $\mathbf{GN} = \mathbf{0}$ and $\mathbf{u}^{\mathrm{n}} \in \mathbb{R}^{N - N_c}$ is the coefficients associated to the null space $\mathbf{N}$. In order to exploit this assumption for the ROM, it is not necessary to explicitly compute the null space $\mathbf{N}$ and the corresponding coefficients $\mathbf{u}^{\mathrm{n}}$ as it will be shown in the next paragraph. More specifically, the approach will be set up such that the term $\mathbf{N}\mathbf{u}^{n}$ is directly approximated using the POD-based method. The decomposition of Equation (1) can then be approximated as:

$$\mathbf{u} \approx \mathbf{u}^{r} = \bar{\mathbf{u}} + \mathbf{B}^{u}\boldsymbol{\alpha}^{u}, \tag{12}$$

where $\mathbf{B}^{u} \in \mathbb{R}^{N\times r}$ is a ROB which allows the ROM to be solved consistently with the displacement $\bar{\mathbf{u}}$ induced by macroscopic deformation and complied with PBC constraints and $\boldsymbol{\alpha}^{u} \in \mathbb{R}^{r}$ are the reduced order degrees-of-freedom. For a given set of displacement $\bar{\mathbf{u}}$, and consistently with the POD approach, a snapshot matrix $\mathbf{S}$ is defined as the collection of solutions (relative to the displacement $\bar{\mathbf{u}}$) of the microscale problem for s parameters:

$$\mathbf{S} = [\mathbf{u}^{1} - \bar{\mathbf{u}},\ \mathbf{u}^{2} - \bar{\mathbf{u}},\ \ldots,\ \mathbf{u}^{s} - \bar{\mathbf{u}}] \in \mathbb{R}^{N\times s}. \tag{13}$$

The POD-based approach identifies a ROB such that the error e defined as:

$$e = \sqrt{\sum_{k=1}^{s} \|(\mathbf{u}^{k} - \bar{\mathbf{u}}) - \mathbf{B}^{u}\boldsymbol{\alpha}^{u,k}\|_{L_2}^{2}} \tag{14}$$

is minimized. The symbol $\|\cdot\|_{L_2}$ stands for the L_2 norm. This allows the best approximation of the snapshot matrix $\mathbf{S}$ in a least square error sense [32]. With the appropriate sets of s design parameters to form the ROB, the obtained ROB can be used further to find the solution to the FOM for any set of design parameters. In practice, the construction of the ROB via POD-based approach involves solving an eigenvalue problem, which allows the use of efficient algorithms to find these reduced order bases [33]. The ROB $\mathbf{B}^{u}$ is obtained by keeping only r eigenvectors ϕ^{i} associated with the r largest eigenvalues μ^{i} of the following eigenproblem:

$$\mathbf{C}\boldsymbol{\phi}^{i} = \mu^{i}\boldsymbol{\phi}^{i}, \tag{15}$$

where $\mathbf{C}$ is the correlation matrix defined by

$$\mathbf{C} = \mathbf{S}\mathbf{S}^{T}. \tag{16}$$

This results in the ROB:

$$\mathbf{B}^{u} = [\boldsymbol{\phi}^{1}\ \boldsymbol{\phi}^{2}\ \ldots\ \boldsymbol{\phi}^{r}]. \tag{17}$$

It is possible to prove that as long as all snapshot samples comply with the constraint matrix $\mathbf{G}$, the resulting ROB $\mathbf{B}^{u}$ also complies with this constraint matrix and is in the span of the null space $\mathbf{N}$ [34], such that:

$$\mathbf{G}\mathbf{B}^{u} = 0. \tag{18}$$

As a result, a ROM can be obtained by substituting the full order displacement $\mathbf{u}$ in Equation (9) by the reduced order approximation in Equation (12) and then performing a Galerkin projection. The resulting ROM is expressed in $\boldsymbol{\alpha}^{u}$:

$$\begin{bmatrix} (\mathbf{B}^{u})^{T} & \mathbf{0} \\ \mathbf{0} & \mathbf{I} \end{bmatrix} \begin{bmatrix} \mathbf{K} & \mathbf{G}^{T} \\ \mathbf{G} & \mathbf{0} \end{bmatrix} \begin{Bmatrix} \bar{\mathbf{u}} + \mathbf{B}^{u}\boldsymbol{\alpha}^{u} \\ \boldsymbol{\lambda} \end{Bmatrix} = \begin{Bmatrix} \mathbf{0} \\ \mathbf{q} \end{Bmatrix}. \tag{19}$$

Using the identity of Equation (18) leads to the following ROM that is independent of the Lagrange multipliers for $\boldsymbol{\alpha}^{u}$, namely

$$(\mathbf{B}^{u})^{T}\mathbf{K}\mathbf{B}^{u}\boldsymbol{\alpha}^{u} = -(\mathbf{B}^{u})^{T}\mathbf{K}\bar{\mathbf{u}} \tag{20}$$

or in short:

$$\mathbf{K}^{r}\boldsymbol{\alpha}^{u} = -(\mathbf{B}^{u})^{T}\mathbf{K}\bar{\mathbf{u}}. \tag{21}$$

The equation (21) is referred to as the *ROM* and is the system of size r instead of size $N + N^{c}$ in the FOM. Since there is no explicitly interest in an (approximate) solution toward $\boldsymbol{\lambda}$, the corresponding equations are omitted. Now that the ROM is constructed, obtaining the solution of a new set of design parameters can be done using the ROM instead. The proposed approach results in the construction of the ROM that can be easily interfaced with any existing third party finite element software. The only information needed from the software is the displacement vector which is the typical output from any software.

3 Application on unidirectional composites

In the preceding section, the elements to implement the projection-based MOR for the general parametrized system are introduced. There are particular challenges that are arisen from applying projection-based MOR to the analysis of UD composites at microscale. The challenges and proposed procedures are detailed in this section. Figure 3 illustrates the overview of MOR implementation to the microscale problem of interest.

3.1 Meshing strategy for utilizing POD approach with various fibre distributions

In this paper, fibre distribution is the parameter of interest. Without strict control on mesh generation, a mesh generator would typically produce the discretized RVEs with different number of nodes even for microstructures with the same RVE size, fibre diameter and number of fibres as shown in Figure 4. In other words, the meshes would be topologically different. Consequently, snapshots from each microstructure may be inconsistent (different number of nodes, different node numbering, etc.). This raises an issue during the construction of ROB via POD procedure because the procedure requires that all snapshots are from the same spatial mesh so that the snapshot matrix can be set up.

A similar situation occurs when POD-based MOR is applied to the snapshots from adaptive FEM [35–37]. Several approaches were proposed to overcome the issue. Fang et al. [35] used a fixed reference mesh where the snapshots were interpolated onto. Gräßle and Hinze [36] constructed the POD basis using the eigensystem of the correlation matrix without the necessity of interpolating snapshots into a common finite element space.

In this work, the concept of a premeshed RVE is proposed. It involves visualizing the possible locations of the fibres in all microstructures that are to be analyzed. All possible locations with the accompanying fibre diameters are then appointed to a RVE, which is subsequently discretized. The resulting mesh has allocated portions where either fibre or matrix properties can be assigned to. This concept is an alternative tailored specifically to the case of fibre distributions in composites. As a consequence, the variation of fibre distribution can be handled without worrying about the spatial discretization of the snapshots. For the example in Figure 5, the constructed mesh offers nine possible positions in which the fibres can be located, as it is shown by the grey areas in Figure 5a. Material property assigned to these grey areas can be interchanged between fibre and matrix. As a result, it is now possible to use the same discretized RVE for different fibre distributions. Figures 5b-5f show the examples of various fibre distributions utilizing the concept of a premeshed RVE.

Generating different fibre distributions on the same discretized RVE is possible because the fibre locations are assumed a priori. Though this could be seen as a limitation, statistical analysis can be performed on the generated fibre distributions to demonstrate that the resulting fibre distributions show varying degree of randomness as seen in Section 4.1.1 for the premeshed RVE considered in this work. For this purpose, the Voronoi polygon and a spatial correlation function called Ripley's K function are used to quantitatively characterize the randomness of the fiber spatial distributions obtained by assigning either matrix or fibre properties to the allotted locations in the premeshed RVE. Pyrz [38] showed that these statistical descriptors are effective in characterizing different fibre patterns. For more details of these statistical descriptors, see Appendix A.

In practice, one might be concerned about the consistency of the results when the computational domain that is discretized for the purpose of employing premeshed RVE. Figure 6 compares the discretization of the matrix phase between the mesh which is used as the premeshed RVE and the conventional mesh in the region where a fibre could be located according to the concept of premeshed RVE. An example of stress distributions is also shown in the figures. In the top figure, small elements are used in the small space between the fiber and the area preserved for a possible fibre. It can be seen that stress distributions look indistinguishable despite the different arrangement of mesh elements.

3.2 Dynamic snapshot selection

For the construction of the ROM, it is important to obtain the ROB that can represent the characteristics of the problem well for the considered parameter space. Conventionally, a set of parameters would be specified in advance. The model associated to each parameter value is analyzed as the FOM. The snapshots from these analyses are then used to obtain a ROB. In this conventional

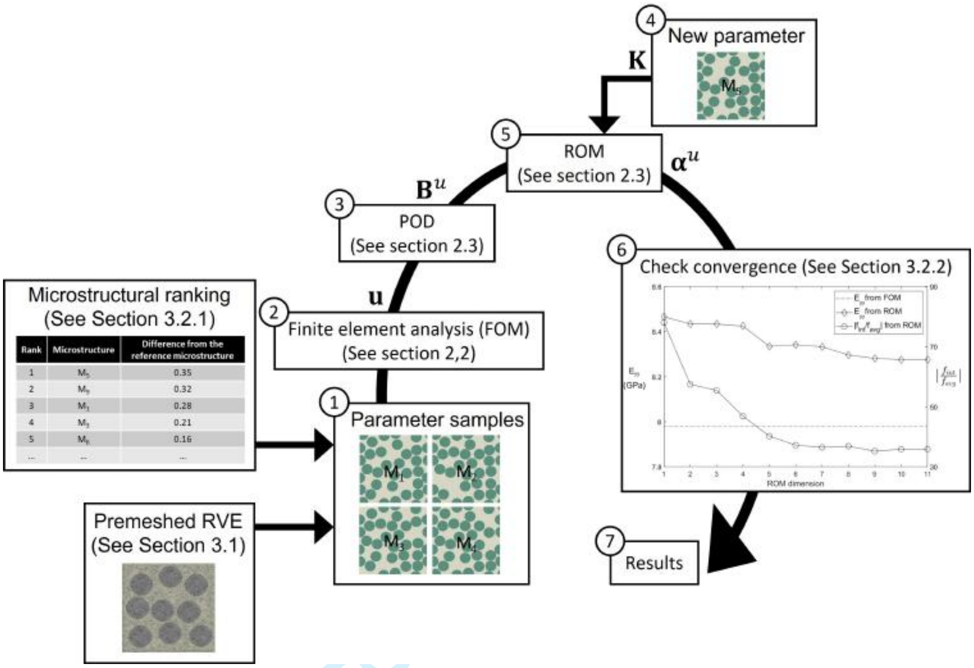

Fig. 3: Procedure of applying projection-based MOR to the analysis of UD composites at microscale

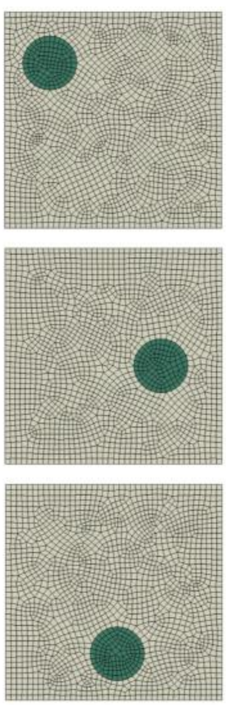

Fig. 4: Discretized RVEs of 1 fibre with 10,500 nodes *(top)*, 9750 nodes *(middle)*, 10,040 nodes *(bottom)*, shown in 2D for clarity

procedure, the ROB is computed only once and used to construct the ROM which is subsequently used for the evaluation of other parameter values. The choice of snapshots to be included in obtaining the ROB is crucial to the quality of the ROM. This leads to a generic MOR issue on how to effectively sample the parameter space.

The snapshots can be selected using a priori sampling methods like random sampling [8], Gaussian processes [8], Sobol sequences [39], among others. They can provide a distribution of points in the parameter space. The drawback is that they do not take into account the characteristics of the problem. Another popular approach for snapshot selection is to couple greedy sampling technique with a posteriori error estimate [40, 41]. The algorithm detects the location in the parameter space where the error from the ROM is the largest. The identified parameter value is subsequently evaluated as the FOM. The ROM is then updated based on the new snapshot. The drawback of the greedy algorithm is in the derivation of problem-specific error estimate. Besides, it is not straightforward to apply these sampling methods when the parametric space is not continuous like the varying fibre distributions. Adaptive sampling is an alternative to these a priori deterministic sampling methods.

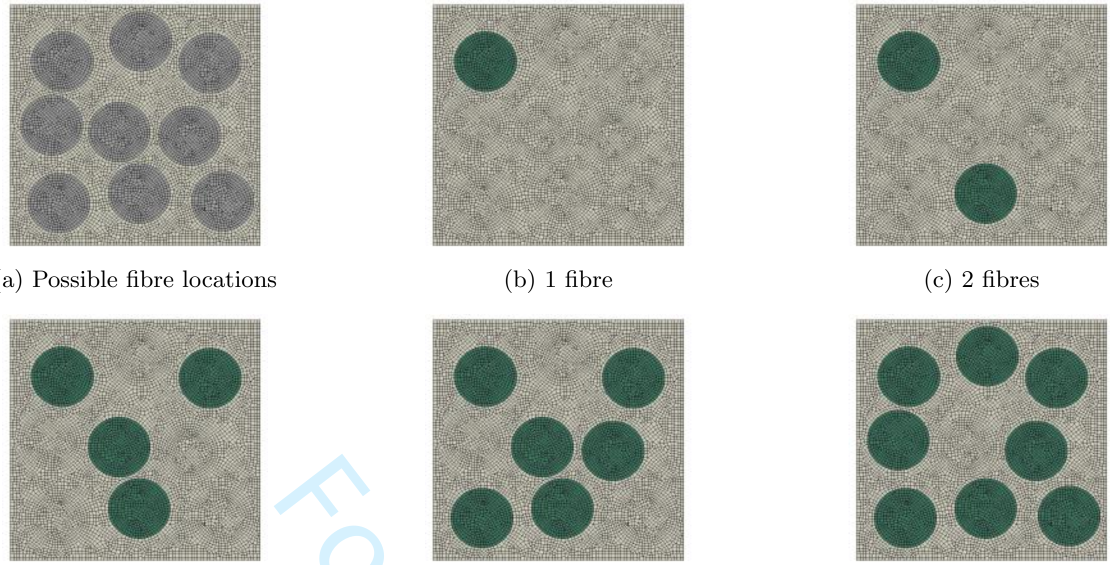

(a) Possible fibre locations (b) 1 fibre (c) 2 fibres

(d) 4 fibres (e) 6 fibres (f) 8 fibres

Fig. 5: Utilization of premeshed RVE

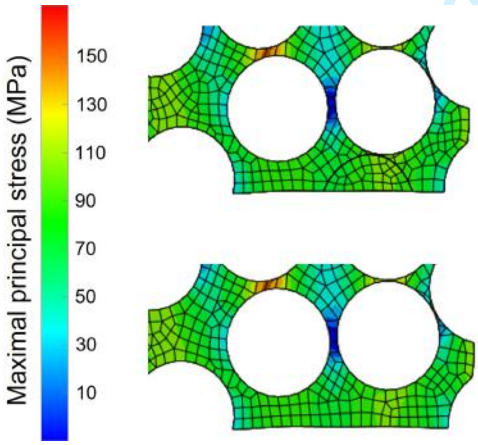

Fig. 6: Discretization in the region where a fibre could be located for the use of premeshed RVE *(top)* and as conventional discretization *(bottom)*

It is an ongoing topic of research in the field of MOR [42, 43].

In this work, the ROB needs to be able to capture the physical behaviour of the composite material with the focus on varying fibre distributions as the parameter space. A dynamic snapshot selection scheme is proposed. In the first stage, it accounts for the differing geometrical characteristic of the microstructures in the construction of ROB through microstructural ranking. Secondly, instead of specifying a set of microstructures in advance for the construction of the ROB, the selection scheme will determine which microstructures should be evaluated as the FOM or as the ROM on-the-fly using two convergence criteria. Once the snapshots are available, they will be used to enrich the ROB gradually and selectively in the evaluation of the subsequent microstructures. The selection scheme features two key elements: (i) microstructural ranking and (ii) convergence criteria, which are detailed in the following subsections.

3.2.1 Microstructural ranking

When constructing the ROB, it is important that the ROB is enriched by varying deformations in the microstructures. The study by Brockenbrough et al.[44] has shown that the tensile and shear deformations are influenced by the fibre distributions. It is thus deduced that the diverse snapshots arise from the diverse microstructures. Microstructures can be distinguished based on their fibre distributions by various statistical descriptors [38]. The benefit of using the statistical descriptors is that there is no need to complete any FOM analyses.

Deciding on which statistical descriptor to use is based on two criteria, its connection to the material response of interest and its computational demand. The distribution of nearest neighbor distances (NND) is chosen to characterize the microstructures. This distribution is defined as the probability of finding the nearest neighbor of each fibre in the microstructure at a particular distance [45]. The study by Hojo et al. [46] shows that the NND between fibres have a substantial effect on the stresses at the fibre/matrix interface, leading to the effect on the overall mechanical properties of the composite. By incorporating the distribution of NND in the process of ROB construction, the ROB will be enriched by the snapshots from dissimilar microstructures. Moreover, the distribution of NND is easy to compute.

The distributions of the NND of two microstructures are shown in Figure 7. When comparing the distributions of the NND, it is possible to quantify how much a microstructure differs from another microstructure. For example, the difference Δ between microstructre M_1 and M_2 illustrated in Figure 8a can be measured as follows

$$\Delta = \sum_{i=1}^{n_{\mathrm{NND}}} \left(\mathcal{P}_{\mathrm{M}_1}(d_i) - \mathcal{P}_{\mathrm{M}_2}(d_i)\right)^2 \qquad (22)$$

where n_{NND} is the total number of normalized NND d, $\mathcal{P}_{\mathrm{M}_1}(d_i)$ and $\mathcal{P}_{\mathrm{M}_2}(d_i)$ are the probability of finding the nearest neighbor at the normalized NND d_i in the microstructure M_1 and M_2, respectively. The NND is normalized by the fibre diameter. All microstructures of interest are compared with the referenced microstructure, which is the one with the shortest distance between all fibres. A larger value of Δ indicates a larger difference between the compared microstructures. The differences are sorted in a descending manner resulting in the microstructural ranking shown in Figure 8b.

Whether evaluated as the FOM or the ROM, the microstructures of interest are to be evaluated following the order in the microstructural ranking rather than following in an arbitrary order. The ROB is meant to be gradually enriched by the snapshot from a microstructure that is different from the previous one. It is worth mentioning that

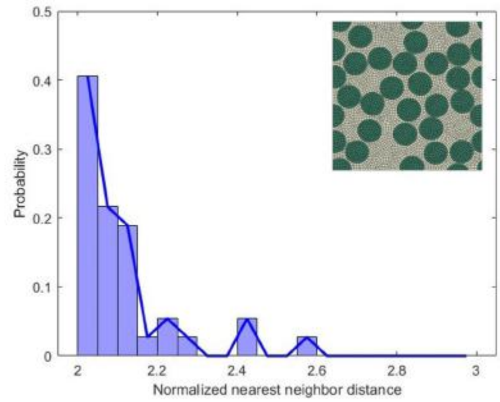

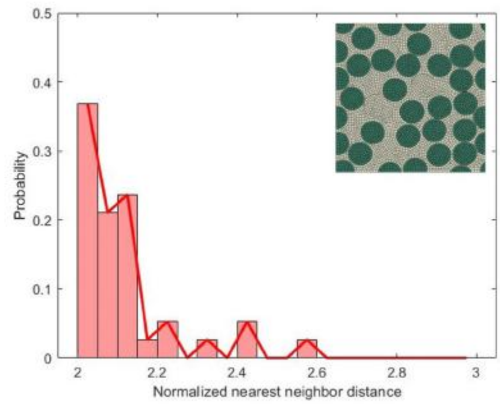

Fig. 7: Distribution of nearest neighbor distance of microstructure M_1 *(top)* and microstructure M_2 *(bottom)*

a microstructural ranking is very cheap to compute since it stems from the simple calculation of distribution of NND between microstructures. It therefore adds only trivial computational cost to the MOR scheme.

3.2.2 Convergence criteria

Once a ROM is constructed and used for the evaluation of a microstructure, it is necessary to decide if the result obtained from the ROM is satisfactory. However, the POD-based approach does not provide any information on the accuracy of the approximated solution obtained from the ROM. A posteriori error estimators were derived for some problems in various research communities [47].

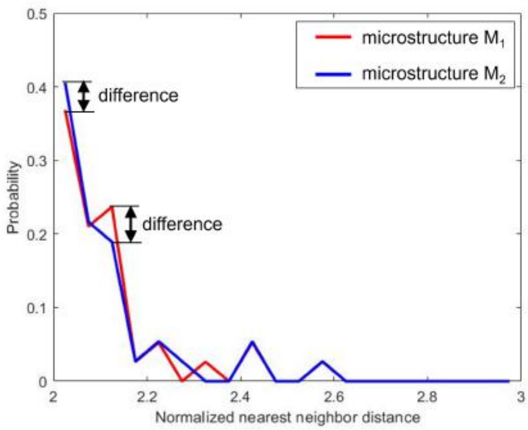

(a) Difference between microstructures

Rank	Microstructure	Difference from the reference microstructure
1	M_5	0.35
2	M_9	0.32
3	M_1	0.28
4	M_3	0.21
5	M_6	0.16
...	...	...

(b) The resulting microstructural ranking

Fig. 8: Summation of differences between two NND distribution in (a) leading to the microstructural ranking in (b)

When it is possible, the derivation of error estimator is generally associated with high theoretical cost and also a problem-specific strategy.

In this work, the monitoring of the convergence of two variables is proposed to serve as a guideline without providing a formal error criterion. Though this convergence monitoring is also a problem-specific strategy, it is a pragmatic scheme based on the physics of the problem and makes use of the available solution from the ROM. The first variable to be monitored is the homogenized elastic properties, whether it be the Young's modulus or shear modulus. For orthotropic material as most composite materials are, these elastic constants can be calculated from the stresses obtained from imposing 6 independent mechanical loads [48]. It appears that the values of the homogenized elastic property obtained from the ROM are approaching a certain value which is in the vicinity of the value obtained from the FOM. An example of converging transverse Young's modulus (E_{yy}) is shown in Figure 9a as a solid line with diamond symbol along with the value from the FOM in dashed line.

Besides monitoring the convergence of the homogenized properties, the second criterion comes from monitoring the internal force (f_{int}) shown as a solid line with circle symbol in Figure 9a. Since the resultant force due to PBCs is only applied at boundary of the domain, the internal force inside the RVE domain equals to zero which is the case for the results from the FOM. For those obtained from the ROM, non-zero values are clearly present as shown in Figures 9b-9d. As the ROM is increasingly enriched (represented by point A to point C in Figure 9a), the non-zero values of the normalized internal force become smaller. The internal force is normalized by the average of the resultant force due to PBCs (f_{avg}). Only the y-component of the normalized internal force is shown here. Similar results are also observed in other components. From this observation, the magnitude of the normalized internal force inside the RVE domain ($|f_{int}/f_{avg}|$) is considered in this work as a convergence indicator together with the homogenized elastic properties. The result from the ROM is accepted as the final solution when the rate of change of both convergence indicators are below a user-specified tolerance. This tolerance is used to control the accuracy of the results from the ROM. It is taken to be 0.01 or 1% rate of change in this study.

Along the process, it is possible that the added snapshot increases the magnitude of the normalized internal force instead as shown in Figure 10a. In this case, the particular snapshot will be excluded from the ROB. The ROM is continued to be enriched by the next available snapshot in the microstructural ranking until the convergence criterion is met or until there is no more available snapshot. When the convergence indicators are still not converged after the available

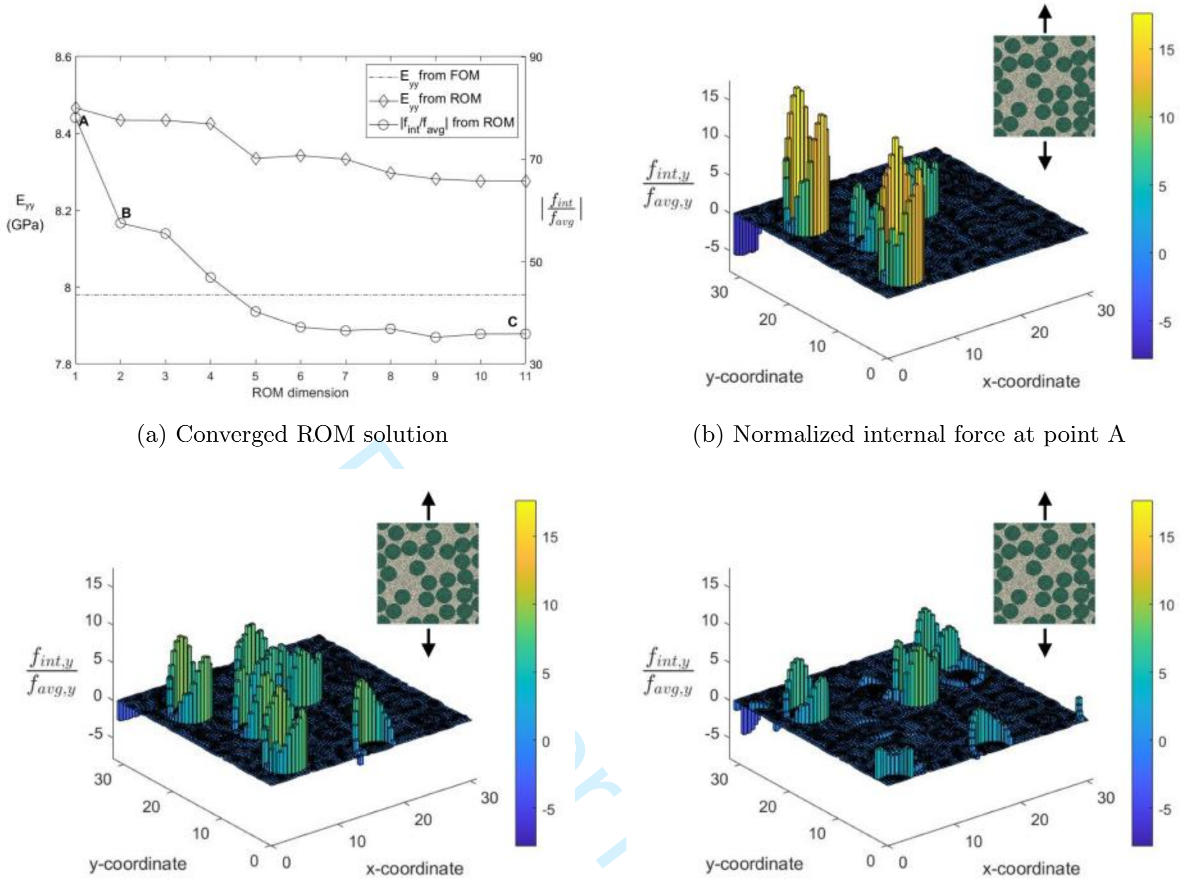

(a) Converged ROM solution (b) Normalized internal force at point A

(c) Normalized internal force at point B (d) Normalized internal force at point C

Fig. 9: Convergence of homogenized properties and internal force in the interior domain of the RVE

snapshots are depleted as shown in Figure 10b, the FOM analysis is thus needed for the given microstructure.

3.2.3 Algorithm

Algorithm 1 outlines the computational process to analyze a set of microstructures and determine which microstructures are to be evaluated as the FOM or the ROM. The algorithm takes as input the microstructural ranking and user-specified tolerance mentioned in sections 3.2.1 and 3.2.2.

In the beginning, the ROM cannot be constructed immediately. The first few microstructures need to be evaluated as the FOM to create the snapshot database. Once the snapshots are available, a ROB can be constructed. The subsequent ROM is used for the evaluation of the microstructure. The homogenized property and internal force from the ROM are checked for convergence. If the convergence criteria are not met, the ROB is enriched step by step by the next snapshot in the microstructural ranking. If the homogenized property and/or the internal force are still not converged after the snapshot database is depleted, the microstrucutre will be evaluted as the FOM.

The proposed algorithm prevents the unnecessary computation of snapshots by dynamically constructing the snapshot database as the evaluation of microstructures is advancing. It can be seen that the selection scheme is embedded coherently in the construction and evaluation of the ROM.

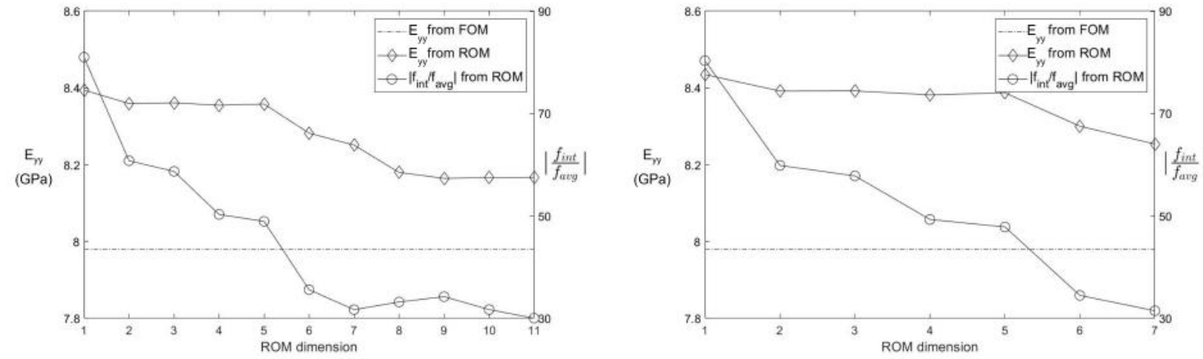

(a) Increase in $\mathsf{f}_{\mathsf{int}}/\mathsf{f}_{\mathsf{avg}}$ (b) Non-converged ROM solution

Fig. 10: Examples of rejected ROM solutions

Algorithm 1 ROM construction embedded with dynamic snapshot selection

```
Generate microstructures M_i (i = 1, ..., m)
Establish microstructural ranking rk                                  ▷ See section 3.2.1
Input user-specified tolerance τ                                      ▷ See section 3.2.2
Initialize displacement collector U to the empty matrix, number of available snapshots n_snapshot = 0
for i = 1, ..., m do
    Set rate of change of the homogenized property r_prop = 100, rate of change of the internal force
    r_f = 100
    if n_snapshot < 2 then
        Run FE simulation of microstructure M_{rk_i} for displacement u  ▷ Solve the FOM
        Update U = U ∪ (u − u^PBC)
        Update n_snapshot = n_snapshot + 1
    else
        Obtain stiffness matrix K of microstructure M_{rk_i}
        Initialize snapshot matrix S to the empty matrix, index j = 1
        while r_prop > τ and r_f > τ and j ≤ n_snapshot do
            Update S = S ∪ U_j
            Construct ROB B̂^u from S                                  ▷ See section 2.3
            Solve the ROM of microstructure M_{rk_i}                   ▷ See equations (12) and (20)
            Compute homogenized property H_j and internal force f_int,j
            if |f_int,j| > |f_int,j−1| then                            ▷ See Figure 10a
                Restore S = S \ U_j
            else
                Update r_prop, r_f
            end if
            Update j = j + 1
        end while
        if r_prop > τ or r_f > τ then                    ▷ When all available snapshots are used
            Run FE simulation of microstructure M_{rk_i}               ▷ Solve the FOM
            Update U = U ∪ (u − u^PBC)
            Update n_snapshot = n_snapshot + 1
        end if
    end if
end for
```

4 Numerical examples

The capability of the proposed approach to reduce computational cost when performing micromechanical analysis of UD composites with fibre distributions as design parameter is demonstrated in this section. The responses from FOM and ROM are compared to assess the accuracy of the proposed approach.

4.1 Microscale model

The RVE at microscale consists of fibres of diameter $d_f = 5\mu$m distributed randomly in the xy-plane as seen in Figure 11. The fibres are positioned randomly using a microstructure generator which is based on a collision model [49, 50]. The generator takes as basic input the number of fibres, fibre diameter, the targeted volume fraction, the minimum distance between fibres, and a seed to initiate the random number generator. The dimension of transverse section l_x and l_y are calculated accordingly. The resulting 2D fibre array is then extruded to build the 3D model and eventually the premeshed RVE. To minimize the computational effort but still maintaining the accuracy, 8 layers of elements are used in the longitudinal direction in such a way that l_z is determined by the element size.

The fibre volume fraction considered in this paper is 59.4%. In order to generate sufficient microstructures at 59.4% fibre volume fraction, the premeshed RVE consists of 100 possible locations of fibre as seen in Figure 11a as the starting point. This allows for the consideration of volume fraction from 0% to 60%. At 59.4% volume fraction, 99 fibres have to be present in the RVE For this particular selection choice, a total of 100 different fibre arrangements with 59.4% volume fraction can be generated having the same discretization. An example of a fibre distribution with 99 fibres used in this study is shown in Figure 11b. The RVE is discretized with 6-node full integration wedge elements and 8-node full integration hexahedral elements. The model has in total 129,680 elements, 180,162 nodes and 540,486 degrees of freedom.

4.1.1 Statistical characteristics of the generated microstructures

The resulting 100 fibre distributions with 59.4% volume fraction generated by using the concept of premeshed RVE were analyzed statistically to characterize their randomness. The degree of randomness is determined in terms of the coefficient of variation from the Voronoi polygons as well as the Ripley's K function. Even though the fibre distributions were generated by assuming the possible fibre locations a priori, the statistics from Voronoi polygons in Table 1 and Figure 12 and the comparison of Ripley's K function of Poisson point pattern and the generated fibre distributions shown in Figure 13 demonstrate the varying degree of randomness in the resulting fibre distributions.

Table 1 shows the coefficient of variation of the areas of Voronoi polygons (ρ_A) and of the distances to neighbouring fibres in Voronoi polygons (ρ_D) for the generated fibre distributions from premeshed RVE and other microstructure generating algorithms. Note that the coefficient of variation is the ratio of the standard deviation to the mean value. As a reference for the degree of randomness in the microstructures, the coefficient of variation obtained from other microstructure generating algorithms are also shown in Table 1. In the literature, the result from only 1 microstructure is available for each Matsuda's method while the average value from 5 microstructures is available for Melro's and Wongsto's methods. It can be seen that both ρ_A and ρ_D from premeshed RVE are comparable to other algorithms. Figure 12 shows the values of ρ_A and ρ_D for all 100 fibre distributions from premeshed RVE. Though some ρ_D are similar, none of ρ_A is the same. Therefore, each combination of ρ_A and ρ_D and hence each fibre distribution from premeshed RVE is unique from the perspective of Voronoi polygons.

Another statistical tool used for distinguishing the pattern of fibre distributions is the Ripley's K function. Figure 13a shows the curve of function $L(h)$ which measures the difference between the Ripley's K function of the Poisson point pattern and those of the generated fibre distributions from premeshed RVE. The curve itself represents the average value while the error bars indicate the range of values for 100 fibre distributions. An example of individual $L(h)$ for 5 fibre distributions

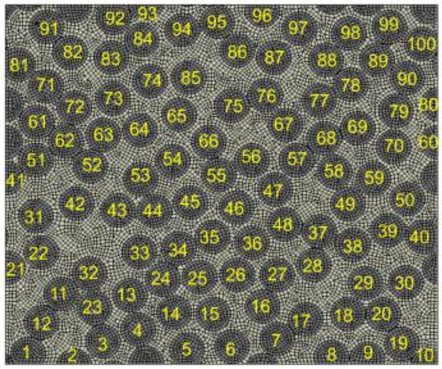

(a) Premeshed RVE with 100 locations of fibre

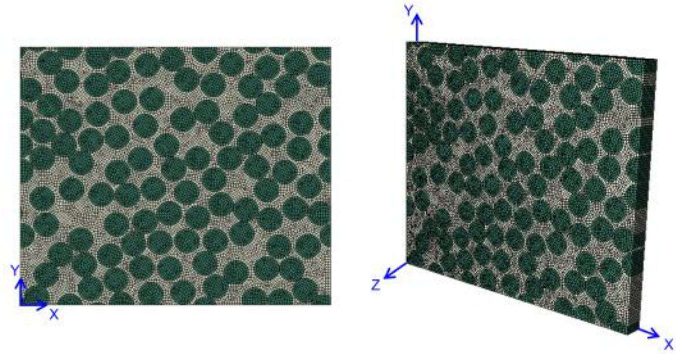

(b) RVE with 99 fibres

Fig. 11: RVEs and mesh detail

Table 1: Coefficient of variation of Voronoi polygons areas and distances to the neighbouring fibres in Voronoi polygons

Microstructure generating approaches	Volume fraction	ρ_A		ρ_D	
		average	range	average	range
premeshed RVE	59.4	0.138	0.123-0.159	0.168	0.157-0.209
Matsuda's Y-distribution [51]	56	0.106	-	0.190	-
Matsuda's point distribution [51]	56	0.135	-	0.256	-
Melro's method [45]	56	0.137	-	0.196	-
Wongsto's method [52]	56	0.129	-	0.190	
Melro's method [45]	65	0.099	-	0.170	-
Wongsto's method [52]	65	0.077	-	0.125	-

is shown in Figure 13b to demonstrate the uniqueness of each curve and hence the fibre distribution from the perspective of the Ripley's K function.

4.1.2 Material properties of the composite constituents

Material properties of fibre and matrix used in this study are listed in Table 2 where E is the Young's modulus, G is the shear modulus, and ν is the Poisson's ratio. The matrix is assumed to be an isotropic linear elastic material which represents a generic epoxy. The fibre is considered as a transverse isotropic linear carbon fibre. Perfect bonding between fibre and matrix is assumed.

4.1.3 Applied loading conditions

To compare the results obtained from FOM and ROM, analyses have been carried out for three load cases:

1. Applying load along the y-axis on the surface perpendicular to the y-axis (termed as transverse tension)
2. Applying load along the y-axis on the surface perpendicular to the x-axis (termed as transverse shear)
3. Applying load along the x-axis on the surface perpendicular to z-axis (termed as in-plane shear)

In all load cases, a prescribed displacement which results in 1% macroscopic strain is applied to the RVE through PBCs. Figure 14 shows the deformed microstructure under these load cases.

Table 2: Material properties of fibre and matrix

Material properties	Carbon fibre [53]	Material properties	Epoxy [54]
$E_{xx} = E_{yy}$ (GPa)	15	E (GPa)	3.76
E_{zz} (GPa)	276	ν (-)	0.39
G_{xz} (GPa)	15		
ν_{xy} (-)	0.3		
ν_{zx} (-)	0.2		

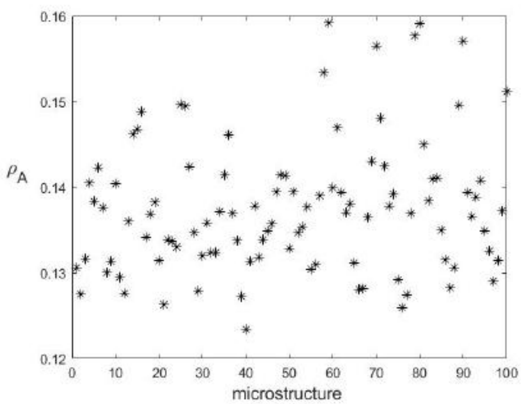

(a) ρ_A from premeshed RVE

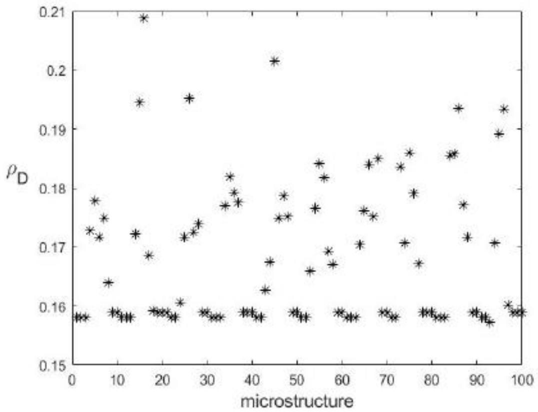

(b) ρ_D from premeshed RVE

Fig. 12: Scattering of coefficient of variation from 100 fibre distributions generated from premeshed RVE

The deformed shapes are magnified by a factor of 10 for a better visualization.

4.2 Computational efficiency

Computational efficiency gained by using the ROM is quantified by two measures, the reduction in model dimension and the reduction in runtime. The computational cost to obtain the displacement vector and the stress field scales with the dimension of the model. By reducing the amount of degrees of freedom, the number of equations to be solved and, consequently, the computational cost also reduce. For the set of 100 fibre distributions considered in this study, the dimension of the FOM and the ROM is shown in Table 3. It can be seen that there is a significant reduction in model dimension by using the ROM.

Table 3: Comparison of model dimension in the FOM and the ROM

Load cases	FOM	ROM
Transverse tension		20 DOFs
Transverse shear	540,486 DOFs	20 DOFs
In-plane shear		12 DOFs

However, there are twofold interpretations behind the dimension of the ROM. For example, for the case of applied transverse tension, 20 out of 100 microstructures were evaluated as the FOM. The rest of the microstructures were solved as a ROM with the dimension no larger than 20. The size of the ROM also reveals how many microstructures are needed to be evaluated as the FOM to provide the information for the ROM construction. It relates to the number of snapshots that are included in the POD procedure. At last, snapshots come from solving the FOM. Table 4 compares the total amount of degrees of freedom involved in evaluating 100 microstructures as (i) the FOM only and (ii) as a combination of the FOM and the ROM according to the proposed MOR scheme for each load case. The amount of DOFs involved in evaluating one microstructure as the ROM does not simply equal to the dimension of the ROM. Evaluating one microstructure does not mean solving the ROM only once. The ROM has to be solved repetitively with increasing size after each iteration until the convergence criteria are met. The amount of DOFs solved in the ROM analysis are consequently accumulated. Nonetheless, the large part of DOFs involved in evaluating microstructures as the ROM comes from acquiring the snapshots.

The reduction in computational time can be seen as well. However, it is important to first clarify that various tasks are executed as part of the FOM and the ROM analysis to obtain the displacement vector and the stress field for one microstructure. The runtime in the FOM analysis can be divided into the time used to assemble the global stiffness matrix and the constraint matrix ('assemble') and the time used to solve the system of linear equations ('solve'). In the ROM analysis, there are two additional tasks included in the runtime which are the time used to construct the ROB ('construct') and the time used to perform Galerkin projection ('project'). Table 5 summarizes the runtime used for each task to evaluate one microstructure. The runtime of the FOM was measured from the reference simulation done by a commercial FE software. For the ROM, the computational time was estimated by measuring the time needed to perform these tasks as a function in a non-optimized in-house MATLAB(R) code. All tasks are run on a laptop Intel(R) Core(TM) i7-8650U processor with 32 GB memory.

From Table 5, it can be seen that the ROM significantly reduces the runtime in solving the system of linear equations due to the small size of the ROM. The share of the runtime spent on running the additional tasks in the ROM case is also very low compared to the solving time in the FOM case. Note that the runtime spent on assembling the global stiffness matrix could be reduced further in the ROM case if an approximation strategy [47] is introduced to establish an affine relation between the global stiffness matrix and the corresponding fibre distribution. Ultimately, the MOR approach requires performing some FOM simulations to set up the ROM. Hence, the total number of microstructures to be evaluated need to reach a certain number to balance this additional cost and achieve the overall runtime speedups as shown in Figure 15. The speedups expect to become even greater when evaluating much larger set of microstructures.

4.2.1 Effect of microstructural ranking on computational efficiency

The effect of evaluating microstructures based on the order in the microstructural ranking is assessed in this section. Two experiments are performed to construct the ROM and to obtain the homogenized properties and the stress distributions. In the first experiment, the order to evaluate microstructures is done according to the microstructural ranking proposed in section 3.2.1. In the second experiment, the order is assigned arbitrarily. The effect of evaluating order on the solution accuracy is negligible. The effect on the computational effort is compared in Table 6 for the case of applied transverse tension in the y-direction. When microstructures were evaluated in an arbitrary order, the algorithm decided to evaluate microstructures as the FOM significantly more. This demonstrates that the ROM is enriched by meaningful snapshots when microstructural ranking is included. The ROM with microstructural ranking achieves an extra gain of about 1.7 times of runtime compared to the ROM with arbitrary order of microstructures as seen in Figure 16.

4.3 ROM verification

Various RVE responses are compared between FOM and ROM to evaluate the mechanical reliability of the proposed MOR scheme. The responses include the prediction of the homogenized elastic properties, the principal stress distributions in the matrix and the interface stress distributions.

4.3.1 Homogenized elastic properties

The responses of 100 different microstructures at 59.4% volume fraction under three load cases are obtained from the FOM and ROM. From these three load cases, the following homogenized elastic properties of the FRP can be extracted: (i) the transverse Young's modulus (E_y), (ii) the transverse shear modulus (G_{xy}) and (iii) the longitudinal shear modulus (G_{xz}). They are determined from the ratio of the relevant homogenized stress and strain under a given loading condition. Predictions of the three moduli obtained from FOM

Table 4: The total amount of degrees of freedom involved in evaluating 100 microstructures

Load cases	DOF involved in evaluating as	
	FOM only	a combination of FOM and ROM
Transverse tension	5.40×10^7	1.08×10^7 as FOM $+1.25 \times 10^4$ as ROM
Transverse shear	5.40×10^7	1.08×10^7 as FOM $+1.16 \times 10^4$ as ROM
In-plane shear	5.40×10^7	6.49×10^6 as FOM $+7.72 \times 10^3$ as ROM

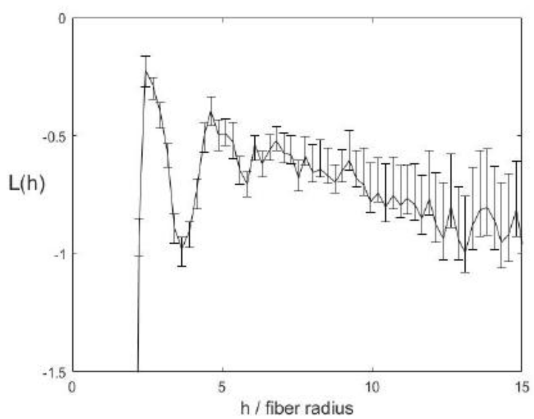

(a) Average $L(h)$ function for 100 fibre distributions

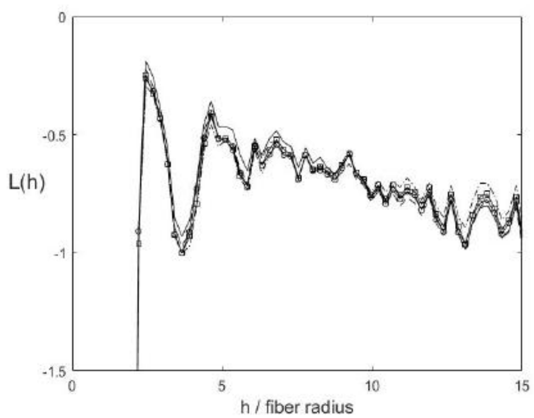

(b) Individual $L(h)$ function for 5 fibre distributions

Fig. 13: Distinguishing the pattern of fibre distributions through the Ripley K's function

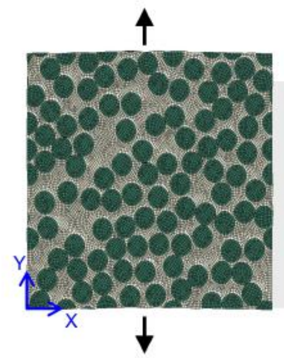

(a) transverse tension

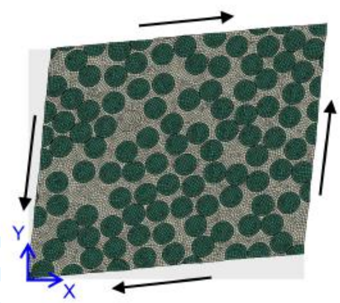

(b) transverse shear

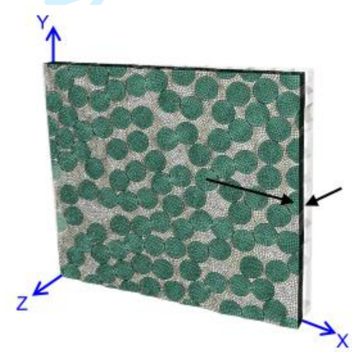

(c) in-plane shear

Fig. 14: Deformation of a microstructure overlapped with undeformed stage

Table 5: The runtime used in solving the FOM and the ROM

Tasks	FOM	ROM
Assemble	70 sec	70 sec
Solve	1950 sec	$\ll$1 sec
Construct	n/a	0.2 sec
Project	n/a	0.6 sec

Table 6: Effect of microstructural ranking on the amount of degrees of freedom involved in evaluating 100 microstructures

Sampling experiment	DOF involved in evaluating
Experiment 1: microstructural ranking	1.08×10^7 as FOM $+1.25 \times 10^4$ as ROM
Experiment 2: arbitrary order	2.00×10^7 as FOM $+2.68 \times 10^4$ as ROM

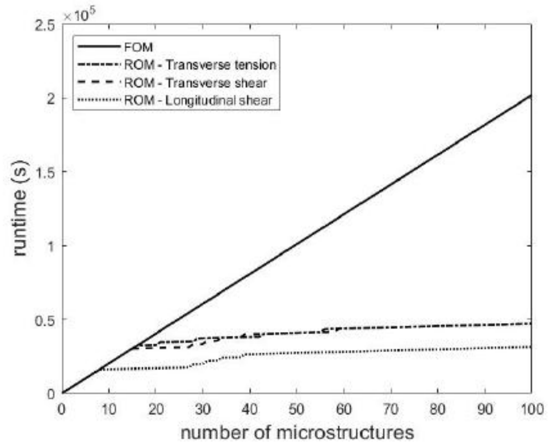

Fig. 15: Accumulated runtime when evaluating 100 microstructures as the FOM or the ROM for different load cases

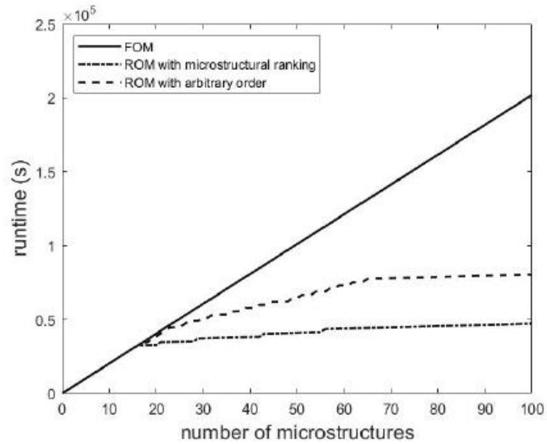

Fig. 16: Comparison of accumulated runtime between the ROM with microstructural ranking and the ROM with arbitrary order

and ROM are listed in Table 7 along with the analytical prediction from Chamis [18].

There is only one single value for each modulus obtained by the analytical model since the Chamis' formulae only accounts for the fibre volume fraction. For those from the FOM and the ROM, the range of modulus values comes from analyzing 100 different fibre distributions. They are not extremely sensitive to the precise distributions of stresses and strains in the RVE of various fibre distributions. They are found to be within a few percent of the average values. Though the values obtained from the ROM are slightly higher than those from the FOM, predictions of the three moduli from the analytical solution, FOM and ROM agree fairly well.

Additionally, the relative differences of the homogenized elastic properties from the FOM and the ROM for each fibre distribution is elaborated in Figure 17. The plots show how many microstructures have the difference between FOM and ROM results fall into a given range. It can be seen that the relative differences of the homogenized elastic properties from the FOM and the ROM are below 7% for all load cases and all microstructures. This shows that the homogenized elastic properties from the FOM and the ROM are in good agreement for 100 different fibre distributions in consideration.

4.3.2 Principal stress distributions

Unlike the homogenized elastic properties, stress distribution is more sensitive to the clustering of the fibres. The maximum principal stress contour plots obtained from the FOM and the ROM are compared in Figure 18 for the applied transverse tension, in Figure 19 for the applied transverse shear, and in Figure 20 for the applied in-plane shear. For each load case, the microstructure with the largest relative difference between the homogenized elastic property from the FOM and the ROM is selected for comparison. For clarity, stress distributions are shown only in the matrix phase.

It can be seen that high stress in the matrix appears where the fibres are clustered, whereas low stress appears in the matrix-rich area. Maximum stresses in the matrix are seen between two fibres that are close to each other in the loading

Table 7: Homogenized elastic properties of the UD fibre reinforced composites at 59.4% fibre volume fraction

Homogenized properties	Chamis	FOM		ROM	
		average	range	average	range
E_y (GPa)	8.90	8.40	8.24-8.57	8.68	8.50-8.80
G_{xy} (GPa)	3.57	2.90	2.84-2.93	2.99	2.91-3.08
G_{xz} (GPa)	4.52	4.45	4.28-4.65	4.67	4.48-4.89

direction. For example, in Figure 19, the highest stress value is located in the area between the fibres with a small distance between them approximately in the 45-deg direction. ROM can capture the overall stress distribution very well. The differences are clearly visible in the areas where the material assignment could be either matrix or fibre. However, these regions are not deemed critical in case of using these patterns to predict damage initiation.

4.3.3 Interface stress distribution

Besides the distribution of maximum principle stress in the matrix, the stress distribution at the fibre/matrix interface around a fibre is investigated in this section. These stresses are crucial information since they contribute to damage initiation and eventually affecting the strength of the composites. Their distributions are also associated with the fibre arrangements in the microstructure. Since damage initiation is likely to occur in regions where the fibres are closer together [44], the fibre pair that has the smallest distance between them is the main focus in this work. One fibre in the pair is selected to demonstrate the capability of the ROM to reproduce the interface stress distribution. Fibre number 53, 52 and 51 are selected to demonstrate this for the case of applied transverse tension, transverse shear and in-plane shear, respectively. Refer to Figure 11a for the fibre numbering.

Stresses in the matrix nodes adjoining the selected fibre are obtained from the FOM and the ROM. The radial stress component (σ_{rr}) normal to the fibre surface and the tangential stress components ($\sigma_{r\theta}, \sigma_{rz}$) along the fibre surface are of interest since they are the relevant components for the damage initiation at the fibre/matrix interface. Each stress component is illustrated in Figure 21. The comparisons of the interface stress around a fibre from the FOM and the ROM are shown in Figure 22 for the case of transverse tension, in Figure 23 for the case of transverse shear, and in Figure 24 for the case of in-plane shear. For each load case, the microstructure with the largest relative difference between the homogenized elastic property from the FOM and the ROM is selected for comparison.

It can be seen in Figures 22-23 that the ROM can capture the distribution of the radial stress σ_{rr} and the tangential shear $\sigma_{r\theta}$ at the fibre/matrix interface very well in terms of the location of the peak value and the asymmetry shape of the curve. Most stress values from the FOM and the ROM are also matching very well. In Figure 22, the ROM produces obvious higher stress at the angle 270 degree. A closer look at this particular fibre distribution from where the results were extracted found that the allocated portion for fibre 64 (see Figure 11a) which is assigned as matrix in this case is in the close vicinity and lies approximately in the loading direction (90 or 270 degree) from fibre 53. This could possibly contribute to the higher stress value from the ROM at 270 degree angle. For the case of applied in-plane shear, the tangential shear σ_{rz} is the only relevant stress component arose along the interface. As shown in Figure 24a, the ROM can also capture the distribution of the tangential shear σ_{rz} well. This illustrates the capability of the ROM to capture material behavior in the out-of-plane direction as well. Similar agreement in the results from the FOM and the ROM is also observed in other fibres.

5 Discussion and conclusion

This paper presents an approach to construct a parametric POD-based ROM capable of predicting the global and local responses of UD-based composite when considering fibre distributions as the design parameter. The proposed framework introduces a premeshed RVE, the microstructural

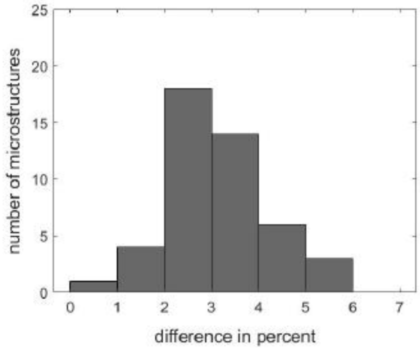

(a) Transverse Young's modulus (E_y)

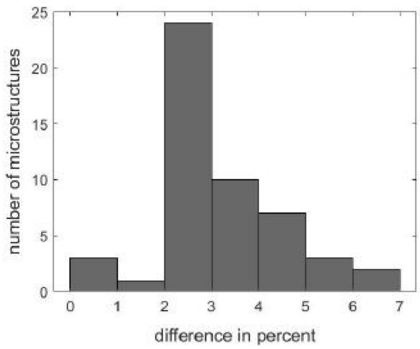

(b) Transverse shear modulus (G_{xy})

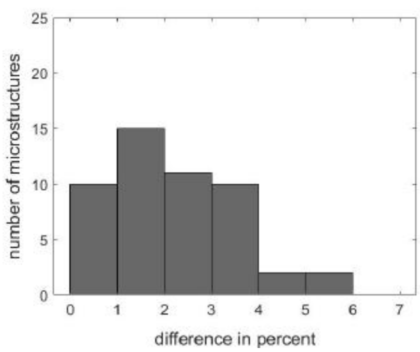

(c) Longitudinal shear modulus (G_{xz})

Fig. 17: Relative differences of the homogenized elastic properties from the FOM and the ROM

ranking and the monitoring of the internal force. The premeshed RVE helps overcome the difficulty encountered in the POD procedure due to the different spatial discretizations. Microstructural ranking accounts for the differing geometrical characteristics in the construction of ROB. Monitoring of the internal force is employed to

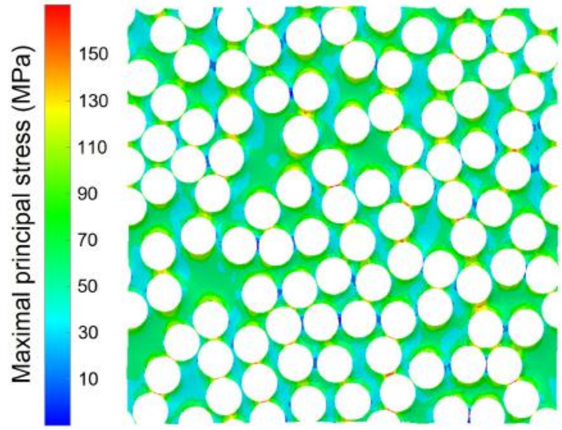

(a) FOM

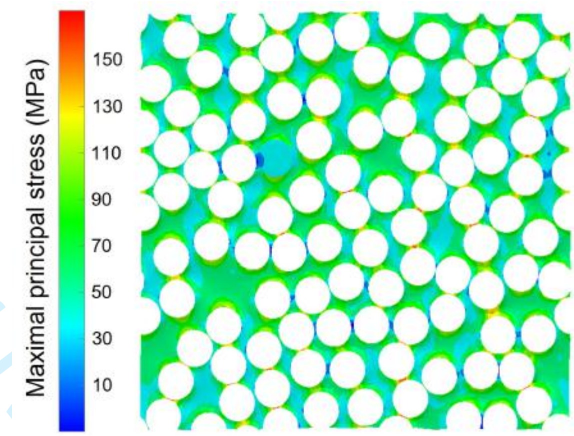

(b) ROM

Fig. 18: Principal stress distributions under transverse tension in y-direction

determine if the solution from the ROM is satisfactory without deriving the theoretical error estimator.

The proposed approach was validated on the microstructures of the UD-based composite subjected to transverse tension, transverse shear and in-plane shear in the elastic regime. The capability of the MOR strategy employed was demonstrated both in terms of homogenized properties and stress states. The accurate prediction of stresses is essential in further studies on damage initiation and propagation in composites. In that sense, this paper sets a solid foundation for the extension on damage and other nonlinear responses affecting the composite integrity. The implemented

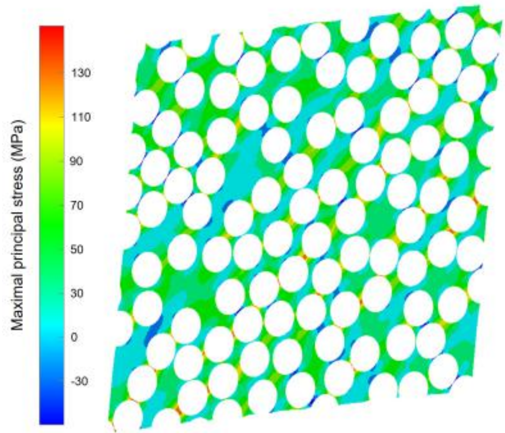

(a) FOM

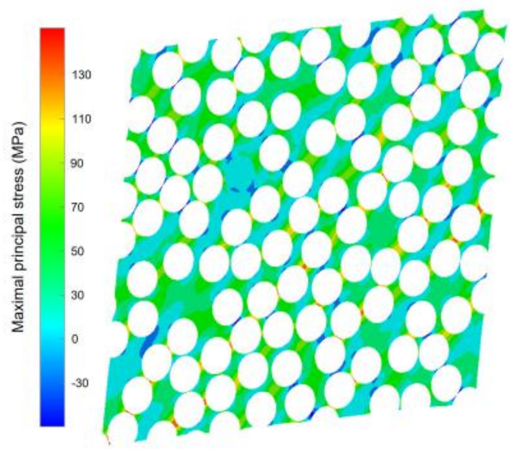

(b) ROM

Fig. 19: Principal stress distributions under transverse shear in xy-direction

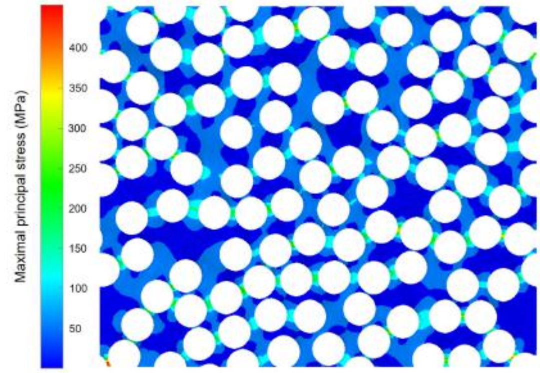

(a) FOM

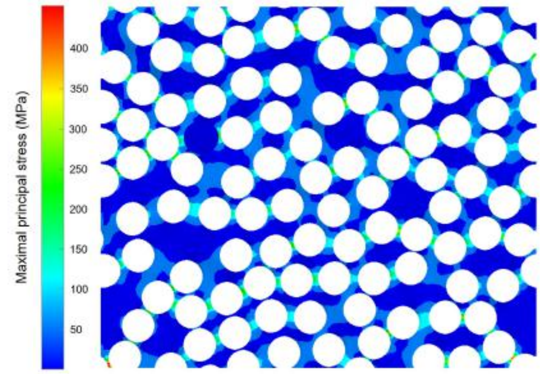

(b) ROM

Fig. 20: Principal stress distributions under in-plane shear in xz-direction

ROM delivered sufficiently accurate global and local responses and a considerable speed up. The success in applying parametric MOR with a varying fibre distribution as parameter space could bridge the gap in the field of MOR for composite materials.

However, certain limitations are acknowledged. First, the ROM was validated on a particular premeshed RVE. A set of microstructures was selected randomly from a limited amount of samples. Different and larger set of microstructures could give an insight to more geometrical characteristics of the microstructures. Secondly, sensitivity analysis on the user-specified tolerance that controls the convergence of the ROM solution should be investigated further. Lastly, the MOR strategy was verified based on the evaluation of microstructures subjected to three independent strains. Verification under more realistic loading conditions is needed since the complex loading such as combined transverse tension and compression could lead to highly localized response developed within the microstructure.

Ongoing research is aiming at extending an application of the introduced MOR approach to include matrix nonlinearity and damage initiation. To deal with the increased complexity in the nonlinear setting, a hyperreduction method [55] will be applied to gain the computational speedup. Future further improvement on computational speedup could be done by exploiting the affine decomposition of the model matrices with respect

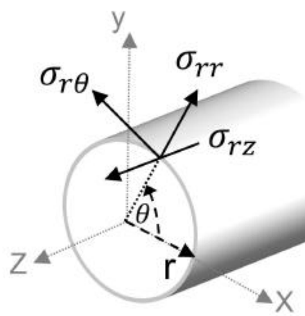

Fig. 21: Stress components at the fibre/matrix interface

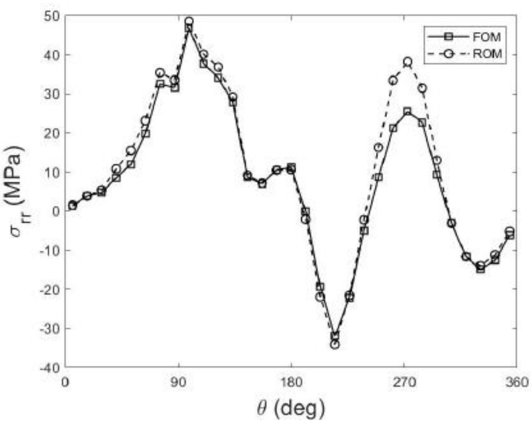

(a) radial stress component (σ_{rr})

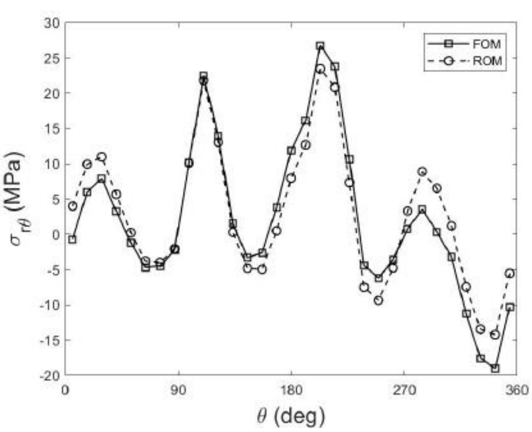

(b) shear stress component ($\sigma_{r\theta}$)

Fig. 22: Interface stress distribution around fibre 53 under transverse tension in y-direction

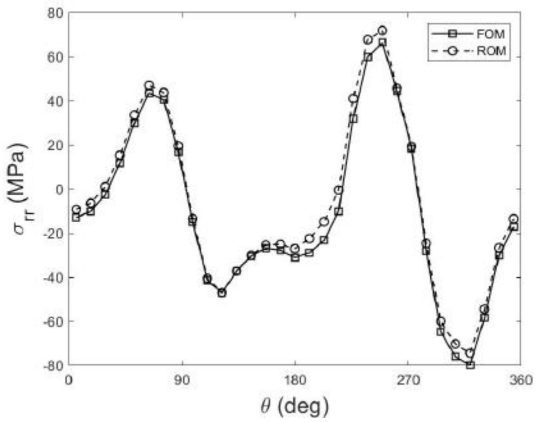

(a) radial stress component (σ_{rr})

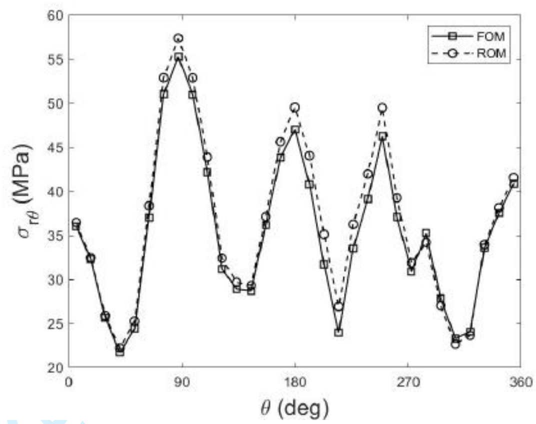

(b) shear stress component ($\sigma_{r\theta}$)

Fig. 23: Interface stress distribution around fibre 52 under transverse shear in xy-direction

to the matrix and fibre properties. Additionally, the approach presented in this paper could introduce the possibility to incorporate different microstructures in the microscale of the (FE^2) framework. To the authors' knowledge, there is no literature in this aspect. Further investigation will be required to see the consequence of using different microstructures and other challenges that could arise.

Credits

A. Jamnongpipatkul: Investigation, Methodology, Software, Validation, Visualization, Writing - original draft. **R.D.B. Sevenois:** Supervision,

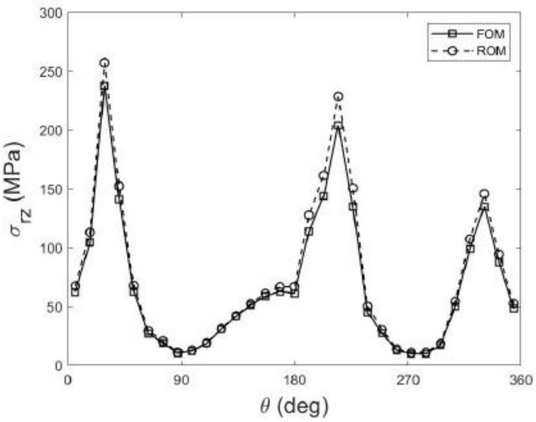

(a) shear stress component (σ_{rz})

Fig. 24: Interface stress distribution around fibre 51 under in-plane shear in xz-direction

Conceptualization, Investigation, Data curation, Writing - review & editing. **W. Desmet:** Funding acquisition, Resources. **F. Naets:** Supervision, Conceptualization, Methodology, Project administration, Writing - review & editing. **F.A. Gilabert:** Supervision, Conceptualization, Software, Data curation, Writing - review & editing.

Acknowledgements

The work leading to this paper has been funded by the SBO project "MOR4MDesign", which fits in the MacroModelMat (M3) research program, coordinated by Siemens (Siemens Digital Industries Software, Belgium), and funded by SIM (Strategic Initiative Materials in Flanders) and VLAIO (Flanders Innovation and Entrepreneurship).

The authors are also grateful to Prof. Wim Van Paepegem for valuable discussions and supplementary managerial support.

References

[1] Sevenois, R.D.B., Garoz, D., Gilabert, F.A., Spronk, S.W.F., Fonteyn, S., Heyndrickx, M., Pyl, L., Van Hemelrijck, D., Degrieck, J., Van Paepagem, W.: Avoiding interpenetrations and the importance of nesting in analytic geometry construction for representative unit cells of woven composite laminates. Compos Sci Technol **136**, 119–132 (2016). https://doi.org/10.1016/j.compscitech.2016.10.010

[2] Zhang, C., Binienda, W.K.: A meso-scale finite element model for simulating free-edge effect in carbon/epoxy textile composite. Mech Mater **76**, 1–19 (2014). https://doi.org/10.1016/j.mechmat.2014.05.002

[3] Kunisch, K., Volkwein, S.: Galerkin proper orthogonal decomposition methods for a general equation in fluid dynamics. SIAM J Numer Anal **40(2)**, 492–515 (2002). https://doi.org/10.1137/S0036142900382612

[4] Zahr, M.J., Avery, P., Farhat, C.: A multi-level projection-based model order reduction framework for nonlinear dynamic multiscale problems in structural and solid mechanics. Int J Numer Meth Engng **112**, 855–881 (2017). https://doi.org/10.1002/nme.5535

[5] Amsallem, D., Zahr, M., Choi, Y., Farhat, C.: Design optimization using hyper-reduced-order models. Struct Multidiscipl Optim **51**, 919–940 (2015). https://doi.org/10.1007/s00158-014-1183-y

[6] Sasikumar, P., Suresh, R., Gupta, S.: Stochastic model order reduction in uncertainty quantification of composite structures. Compo Struct **128**, 21–34 (2015). https://doi.org/10.1016/j.compstruct.2015.03.045

[7] Solder, D., Brands, B., Zabilhyan, R., Steinmann, P., Mergheim, J.: A numerical study of different projection-based model reduction techniques applied to computational homogenisation. Comput Mech **60**, 613–625 (2017). https://doi.org/10.1007/s00466-017-1428-x

[8] Goury, O., Amsallem, D., Bordas, S.P.A., Liu, W.K., Kerfriden, P.: Automatised selection of load paths to construct reduced-order models in computational damage micromechanics: from dissipation-driven random selection to bayesian optimization. Comput Mech **58**, 213–234 (2016). https://doi.org/10.1007/s00466-016-1290-2

[9] Tuijl, R.A., Remmers, J.J.C., D., G.M.G.: Integration efficiency for model reduction in micro-mechanical analyses. Comput Mech **62**, 151–169 (2018). https://doi.org/10.1007/s00466-017-1490-4

[10] Raschi, M., Lloberas-Valls, O., Huespe, A., Oliver, J.: High performance reduction technique for multiscale finite element modeling (hpr-fe^2): Towards industrial multiscale fe software. Comput Methods Appl Mech Eng **375**, 113580 (2021). https://doi.org/10.1016/j.cma.2020.113580

[11] Ghayoor, H., Marsden, C.C., Hoa, S.V., Melro, A.R.: Numerical analysis of resin-rich areas and their effects on failure initiation of composites. Compos Part A Appl **117**, 125–133 (2019). https://doi.org/10.1016/j.compositesa.2018.11.016

[12] Ghayoor, H., Hoa, S.V., Marsden, C.C.: A micromechanical study of stress concentrations in composites. Compos B Eng **132**, 115–124 (2018). https://doi.org/10.1016/j.compositesb.2017.09.009

[13] Chen, X., Papathanasiou, T.D.: Interface stress distributions in transversely loaded continuous fiber composites: Parallel computation in multi-fiber rves using the boundary element method. Compos Sci Technol **64**, 1101–1114 (2004). https://doi.org/10.1016/j.compscitech.2003.07.006

[14] Sudhit, A., Talreja, R.: Simulation of manufacturing induced fiber clustering and matrix voids and their effect on transverse crack formation in unidirectional composites. Compos Part A Appl Sci Manuf **127**, 105620 (2019). https://doi.org/10.1016/j.compositesa.2019.105620

[15] Zhang, L., Ernst, L.J., Brouwer, H.R.: Transverse behaviour of a unidirectional composite (glass fibre reinforced unsaturated polyester.) part i. influence of fibre packing geometry. Mech Mater **27**, 13–36 (1998). https://doi.org/10.1016/S0167-6636(97)00040-9

[16] Huang, Y., Jin, K.K., Ha, S.K.: Effects of fiber arrangement on mechanical behavior of unidirectional composites. J Compos Mater **42(18)**, 1851–1871 (2008). https://doi.org/10.1177/0021998308093910

[17] Halpin, J.C., Kardos, J.L.: The halpin-tsai equations: a review. Polym Eng Sci **16**, 344–352 (1976). https://doi.org/10.1002/pen.760160512

[18] Chamis, C.C.: Mechanics of composite materials: Past, present and future. J Compos Technol Res **11**, 3–14 (1989). https://doi.org/10.1520/CTR10143J

[19] Terada, K., Hori, M., Kyoya, T., Kikuchi, N.: Simulation of the multi-scale convergence in computational homogenization approaches. Int J Solids Struct **37**, 2285–2311 (2000). https://doi.org/10.1016/S0020-7683(98)00341-2

[20] Trias, D., Costa, J., Turon, A., Hurtado, J.: Determination of the critical size of a statistical representative volume element (srve) for carbon reinforced polymers. Acta Mater **54(13)**, 3471–3484 (2006). https://doi.org/10.1016/j.actamat.2006.03.042

[21] Jiménez, F.L.: Variations in the distribution of local strain energy within different realizations of a representative volume element. Compos B Eng **176**, 107111 (2019). https://doi.org/10.1016/j.compositesb.2019.107111

[22] Yin, S., Pindera, M.J.: Homogenized moduli and local stress fields of random fiber composites under homogeneous and periodic boundary conditions. Eur J Mech A Solids **93**, 104504 (2022). https://doi.org/10.1016/j.euromechsol.2022.104504

[23] Monteiro, E., Yvonnet, J., He, Q.C.: Computational homogenization for nonlinear conduction in heterogeneous materials using model reduction. Comput Mater Sci **42**, 704–712 (2008). https://doi.org/10.1016/j.commatsci.2007.11.001

[24] Yvonnet, J., He, Q.C.: The reduced model multiscale method (r3m) for the non-linear homogenization of hyperelastic media at finite strains. J Comput Phys **223(1)**,

341–368 (2007). https://doi.org/10.1016/j.jcp.2006.09.019

[25] Geers, M.G.D., Kouznetsova, V.G., Brekelmans, W.A.M.: Multi-scale computational homogenization: Trends and challenges. J Comput Appl Math **234**, 2175–2182 (2010). https://doi.org/10.1016/j.cam.2009.08.077

[26] Hill, R.: On constitutive macro-variables for heterogeneous solids at finite strain. Proc R Soc London A **326 (1565)**, 131–147 (1972). https://doi.org/10.1098/rspa.1972.0001

[27] Mandel, J.: Plasticite Classique, Viscoplasticite, 1st edn. Springer, Vienna (1972)

[28] Miehe, C., Koch, A.: Computational micro-to-macro transitions of discretized microstructures undergoing small strains. Arch Appl Mech **72**, 300–317 (2002). https://doi.org/10.1007/s00419-002-0212-2

[29] LLorca, J., González, C., Molina-Aldareguía, J.M., Segurado, J., Seltzer, R., Sket, F., Rodríguez, M., Sábada, S., Muñoz, R., Canal, L.P.: Multiscale modeling of composite materials: a roadmap towards virtual testing. Adv Mater **23**, 5130–5147 (2011). https://doi.org/10.1002/adma.201101683

[30] Garoz, D., Gilabert, F.A., Sevenois, R.D.B., Spronk, S.W.F., Van Paepegem, W.: Consistent application of periodic boundary conditions in implicit and explicit finite element simulations of damage in composites. Compos B Eng **168**, 254–266 (2019). https://doi.org/10.1016/j.compositesb.2018.12.023

[31] Cook, R.D., Malkus, D.S., Plesha, M.E., Witt, R.J.: Concepts and Applications of Finite Element Analysis, 4th edn. John Wiley & Sons Inc, Hoboken, NJ (2001)

[32] Liang, Y.C., Lee, H.P., Lim, S.P., Lin, W.Z., Lee, K.H., Wu, C.G.: Proper orthogonal decomposition and its applications - part i: theory. J Sound Vib **252(3)**, 527–544 (2002). https://doi.org/10.1006/jsvi.2001.4041

[33] Quarteroni, A., Manzoni, A., Negri, F.: Reduced Basis Methods for Partial Differential Equations: An Introduction, 1st edn. Springer, Cham, Switzerland (2016). https://doi.org/10.1007/978-3-319-15431-2

[34] Naets, F., Devos, T., Humer, A., Gerstmayr, J.: A noninvasive system-level model order reduction scheme for flexible multibody simulation. Int J Numer Meth Engng **121**, 3083–3107 (2020). https://doi.org/10.1002/nme.6348

[35] Fang, F., Pain, C.C., Navon, I.M., Piggott, M.D., Gorman, G.J., Allison, P.A., Goddard, A.J.: Reduced-order modelling of an adaptive mesh ocean model. Int J Numer Meth Fluids **59**, 827–851 (2009). https://doi.org/10.1002/fld.1841

[36] Gräßle, C., Hinze, M.: Pod reduced-order modeling for evolution equations utilizing arbitrary finite element discretizations. Adv Comput Math **44**, 1941–1978 (2018). https://doi.org/10.1007/s10444-018-9620-x

[37] Ullmann, S., Rotkvic, M., Lang, J.: Pod-galerkin reduced-order modeling with adaptive finite element snapshots. J Comput Phys **325**, 244–258 (2016). https://doi.org/10.1016/j.jcp.2016.08.018

[38] Pyrz, R.: Correlation of microstructure variability and local stress field in two-phase materials. Mater Sci Eng **A177**, 253–259 (1994). https://doi.org/10.1016/0921-5093(94)90497-9

[39] Bessa, M.A., Bostanabad, R., Liu, Z., Hu, A., W., A.D., Brinson, C., Chen, W., Liu, W.K.: A framework for data-driven analysis of materials under uncertainty: countering the curse of dimensionality. Comput Methods Appl Mech Eng **320**, 633–667 (2017). https://doi.org/10.1016/j.cma.2017.03.037

[40] Veroy, K., Patera, A.T.: Certified real-time solution of the parametrized steady incompressible navier-stokes equations: rigorous reduced-basis a posteriori error bounds. Int J Numer Meth Fluids **47(8-9)**, 773–788 (2005). https://doi.org/10.1002/fld.867

[41] Paul-Dubois-Taine, A., Amsallem, D.: An adaptive and efficient greedy procedure for the optimal training of parametric reduced-order models. Int J Numer Methods Eng **102(5)**, 1262–1292 (2015). https://doi.org/10.1002/nme.4759

[42] Oxberry, G.M., Kostova-Vassilevska, T., Arrighi, W., Chand, K.: Limited-memory adaptive snapshot selection for proper orthogonal decomposition. Int J Numer Meth Engng **109**, 198–217 (2017). https://doi.org/10.1002/nme.5283

[43] Peherstorfer, B.: Model reduction for transport-dominated problems via online adaptive bases and adaptive sampling. SIAM J Sci Comput **42(5)**, 2803–2836 (2020). https://doi.org/10.1137/19M1257275

[44] Brockenbrough, J.R., Suresh, S., Wienecke, H.A.: Deformation of metal-matrix composites with continuous fibers: geometrical effects of fiber distribution and shape. Acta Metall Mater **39(5)**, 735–752 (1991). https://doi.org/10.1016/0956-7151(91)90274-5

[45] Melro, A.R., Camanho, P.P., Pinho, S.T.: Generation of random distribution of fibers in long-fiber reinforced composites. Compos Sci Technol **68**, 2092–2102 (2008). https://doi.org/10.1016/j.compscitech.2008.03.013

[46] Hojo, M., Mizuno, M., Hobbiebrunken, T., Adachi, T., Tanaka, M., Ha, S.K.: Effect of fiber array irregularities on microscopic interfacial normal stress states of transversely loaded ud-cfrp from viewpoint of failure initiation. Compos Sci Technol **69**, 1726–1734 (2009). https://doi.org/10.1016/j.compscitech.2008.08.032

[47] Benner, P., Gugercin, S., Wilcox, K.: A survey of projection-based model reduction methods for parametric dynamical systems. SIAM Rev **57(4)**, 483–531 (2015). https://doi.org/10.1137/130932715

[48] Torquato, S.: Random Heterogeneous Materials: Microstructure and Macroscopic Properties, 1st edn. Springer, New York, NY (2002). https://doi.org/10.1007/978-1-4757-6355-3

[49] Knott, G.M., Jackson, T.I., Buckmaster, J.: Random packing of heterogeneous propellants. AIAA J **39(4)**, 678–686 (2001). https://doi.org/10.2514/2.1361

[50] Lubachevsky, B.D., Stillinger, F.H.: Geometric properties of random disk packings. J Stat Phys **60(5-6)**, 561–583 (1990). https://doi.org/10.1007/BF01025983

[51] Matsuda, T., Ohno, N., Tanaka, H., Shimizu, T.: Effects of fibre distribution on elastic-viscoplastic behavior of long fibre-reinforced laminates. Int J Mech Sci **45(10)**, 1583–1598 (2003). https://doi.org/10.1016/j.ijmecsci.2003.09.021

[52] Wongsto, A., Li, S.: Micromechanical finite element analysis of unidirectional fibre-reinforced composites with fibres distributed at random over the transverse cross-section. Compos Part A Appl **36(9)**, 1246–1266 (2005). https://doi.org/10.1016/j.compositesa.2005.01.010

[53] Arteiro, A., Catalanotti, G., Melro, A.R., Linde, P., Camanho, P.P.: Micro-mechanical analysis of the in situ effect in polymer composite laminates. Compo Struct **116**, 827–840 (2014). https://doi.org/10.1016/j.compstruct.2014.06.014

[54] Fiedler, B., Hojo, M., Ochiai, S., Schulte, K., Ando, M.: Failure behavior of an epoxy matrix under different kinds of static loading. Compos Sci Technol **61(11)**, 1615–1624 (2001). https://doi.org/10.1016/S0266-3538(01)00057-4

[55] Farhat, C., Avery, P., Chapman, T., Cortial, J.: Dimensional reduction of nonlinear finite element dynamic models with finite rotations and energy-based mesh sampling and weighting for computational efficiency. Int J Numer Meth Engng **98**, 625–662 (2014). https://doi.org/10.1002/nme.4668

[56] Liu, K.C., Ghoshal, A.: Validity of random microstructures simulation in fiber-reinforced composite materials. Compos B Eng **57**, 56–70 (2014). https://doi.org/10.1016/j.compositesb.2013.08.006

[57] Pyrz, R.: Quantitative description of the microstructure of composites. part i: morphology of unidirectional composite systems. Compos Sci Technol **50(2)**, 197–208 (1994). https://doi.org/10.1016/0266-3538(94)90141-4

[58] Ripley, B.D.: Modelling spatial patterns. J Roy Stat Soc Ser B **39(2)**, 172–212 (1977). https://doi.org/10.1111/j.2517-6161.1977.tb01615.x

[59] Diggle, P.: Statistical Analysis of Spatial Point Patterns, 2nd edn. Hodder Education Publishers, London, UK (2003)

A Statistical tools for characterizing the generated microstructures from premeshed RVE

In order to quantitatively characterize the spatial distributions of fibres, statistical descriptors like Voronoi polygons and Ripley's K function can be used.

A.1 Voronoi polygons

Dirichlet tessellation seek to construct an n-sided polygon around each fibre center in which the perimeter is equidistant between two neighboring fibres [56]. This polygon is named Voronoi polygon. The standard deviation of the areas of the Voronoi polygons defines the more or less periodic distribution of fibres. In a periodic distribution, all Voronoi polygons are equal and the standard deviation of the areas is therefore zero. From Voronoi polygons, it is also possible to calculate the average of the distances between one given fibre and its neighbouring fibres. A neighbouring fibre is one that shares a side of the Voronoi polygon with the fibre of interest. This measure provides information on how separate from each other the fibres are. Like the standard deviation of the areas of Voronoi polygons, the standard deviation of the neighbouring distances in Vornoi polygons is zero in a periodic distribution [45]. An example of the Voronoi polygons is shown in Figure 25.

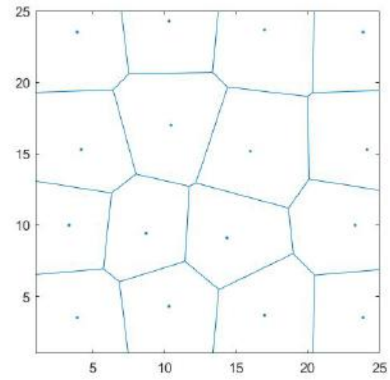

Fig. 25: Voronoi polygons generated from Dirichlet tessellation for 16 centers

A.2 Ripley's K function

The second order intensity function, also known as Ripley's K function ($K(h)$), can be used to distinguish between different types of point patterns [57]. The function is given by [58]:

$$K(h) = \frac{A}{N^2} \sum_{k=1}^{N} w_k^{-1} I_k(h), \qquad (23)$$

where N is the number of fibres (points) in the observation area A, $I_k(h)$ is the number of other fibre centers lying within radial distance h of the center of a given fibre k, and w_k is the correction factor that accounts for the fibres that intersect the edges of the observation area. The correction factor is defined as the proportion of the circumference of the circle of radius h that is contained within the observation area. The $K(h)$ of any fibre distributions can be compared with the completely spatial randomness of the Poisson point pattern. Ripley's K function for the Poisson point pattern $K_p(h)$ can be evaluated analytically [59]:

$$K_p(h) = \pi h^2. \qquad (24)$$

The functions (23) and (24) can be compared using the following relation [45]:

$$L(h) = \frac{K(h)}{\pi} - h. \qquad (25)$$